JGR Solid Earth

RESEARCH ARTICLE
10.1029/2019JB017793

Imaging the Shallow Subsurface Structure of the North Hikurangi Subduction Zone, New Zealand, Using 2-D Full-Waveform Inversion

Melissa Gray[1], Rebecca E. Bell[1], Joanna V. Morgan[1], Stuart Henrys[2], Daniel H. N. Barker[2], and the IODP Expedition 372 and 375 science parties

[1]Department of Earth Science and Engineering, Imperial College London, London, UK, [2]GNS Science, Lower Hutt, New Zealand

Key Points:
- Full-waveform inversion was used to produce a high-resolution *P* wave velocity model of the upper ~2 km of the north Hikurangi subduction zone
- Recovered velocities and gradients correlate well with drilled sonic logs, suggesting that the details we see in our FWI velocity models are real
- Velocity changes across faults may relate to compaction, and in some cases low velocities along faults may indicate conduits for fluid flow

Supporting Information:
- Supporting Information S1

Correspondence to:
M. Gray,
m.gray15@imperial.ac.uk

Citation:
Gray, M., Bell, R. E., Morgan, J. V., Henrys, S., Barker, D. H. N., & the IODP Expedition 372 and 375 science parties (2019). Imaging the shallow subsurface structure of the north Hikurangi subduction zone, New Zealand, using 2-D full-waveform inversion. *Journal of Geophysical Research: Solid Earth*, *124*, 9049–9074. https://doi.org/10.1029/2019JB017793

Received 8 APR 2019
Accepted 27 JUL 2019
Accepted article online 13 AUG 2019
Published online 30 AUG 2019

Abstract The northern Hikurangi plate boundary fault hosts a range of seismic behaviors, of which the physical mechanisms controlling seismicity are poorly understood, but often related to high pore fluid pressures and conditionally stable frictional conditions. Using 2-D marine seismic streamer data, we employ full-waveform inversion (FWI) to obtain a high-resolution 2-D *P* wave velocity model across the Hikurangi margin down to depths of ~2 km. The validity of the FWI velocity model is investigated through comparison with the prestack depth-migrated seismic reflection image, sonic well data, and the match between observed and synthetic waveforms. Our model reveals the shallow structure of the overriding plate, including the fault plumbing system above the zone of slow-slip events to theoretical resolution of a half seismic wavelength. We find that the hanging walls of thrust faults often have substantially higher velocities than footwalls, consistent with higher compaction. In some cases, intrawedge faults identified from reflection data are associated with low-velocity anomalies, which may suggest that they are high-porosity zones acting as conduits for fluid flow. The continuity of velocity structure away from International Ocean Discovery Program drill site U1520 suggests that lithological variations in the incoming sedimentary stratigraphy observed at this site continue to the deformation front and are likely important in controlling seismic behavior. This investigation provides a high-resolution insight into the shallow parts of subduction zones, which shows promise for the extension of modeling to 3-D using a recently acquired, longer-offset, seismic data set.

1. Introduction

The Hikurangi plate boundary fault offshore the east coast of the North Island, New Zealand, exhibits a range of seismic behavior ranging from stick-slip to aseismic creep. Perhaps most notably, the north Hikurangi plate boundary fault experiences slow-slip events (SSEs) every 18–24 months, identified using continuous GPS (cGPS) data (Wallace et al., 2012; Wallace et al., 2016; Wallace & Beavan, 2010). Recent results from absolute pressure gauges (APGs) offshore indicate that SSEs at north Hikurangi occur at depths as shallow as 2 km below the seafloor and may even propagate to the seafloor in some areas, making them some of the most well-characterized, shallow recorded SSEs worldwide (Wallace et al., 2016).

The fact that the northern Hikurangi margin experiences such regular SSEs has led to speculation about the physical properties at the margin including fluid presence. Some laboratory experiments and numerical models suggest that slow slip may be more likely to occur when pore pressures reach near-lithostatic levels (Audet et al., 2010; Liu & Rice, 2005; Liu & Rice, 2007; Shibazaki & Iio, 2003; Song et al., 2009). This view is supported by evidence in seismic data for the presence of fluids at several margins where slow slip occurs, for example, at Nankai (Bangs et al., 2009; Kamei et al., 2012; Tobin & Saffer, 2009), Costa Rica (Bangs et al., 2014; Saffer, 2003; Sahling et al., 2008), and Cascadia (Rogers & Dragert, 2003; Wech et al., 2009). We might therefore expect a complex fault plumbing system at the margin above regions where slow slip is known to occur.

Reflection seismic data acquired across subduction zones provide information on impedance contrasts (the product of velocity and density) between subsurface layers. Fluid presence has previously been interpreted within plate boundary zones or within splay faults on the basis of polarity reversals and brightness of reflections observed from seismic sections (Bangs et al., 1999; Bell et al., 2014; Rondenay et al., 2008); however,

these observations are indirect indicators of fluids. Alternatively, it has been suggested that variations in frictional behavior are required to promote SSEs (Ikari & Saffer, 2011). A mixture of rheology, potentially caused by very heterogeneous lithology within the fault zone or within the incoming section, could be one mechanism to produce such conditionally frictionally stable conditions (Fagereng & Sibson, 2010). Recovering physical properties at high resolution at the margin could provide insight into fault mechanisms, fluid presence, and incoming lithology at the margin, which may all potentially affect seismicity. Drilling data are also required to develop relationships between rock properties and elastic properties at drill sites to further understand the relationships between physical properties and seismicity at the margin.

At northern Hikurangi, Bell et al. (2010) have suggested that high-amplitude reflections in the zone of maximum cumulative slow slip since 2002 could indicate fluid presence and potentially high fluid pressure. However, this interpretation is solely based on the high amplitude of reflections at depth, which may also be caused by lithological variations. Regional earthquake tomography at Hikurangi, including Vp/Vs ratios (Eberhart-Phillips & Chadwick, 2002), provides low-resolution models of physical properties (grid spacing >10 km offshore). Barker et al. (2018) have developed a velocity model by conducting prestack depth migration (PSDM) across the margin and concluded that wave speeds in the zone of high-amplitude reflections are 7% lower than the surrounding strata. This finding supports the interpretation of high fluid pressures within subducting sediments, which may facilitate SSEs at northern Hikurangi; however, the presence of a low-velocity lithology within the fault zone cannot be yet ruled out. Recently, two International Ocean Discovery Program (IODP) Expeditions—372 and 375—have collected logging while drilling (LWD) and wireline data, as well as core samples from four drill sites across the margin (Figure 1; Pecher et al., 2019; Wallace et al., 2019), which provide direct constraints on physical properties. However, these data are limited in depth to 750 m below seafloor (mbsf) for the LWD data, 946 mbsf for the wireline, and 1,054 mbsf for the core data, but they provide an insight into the velocity structure, porosity, and fluid properties at isolated locations.

Full-waveform inversion (FWI) is an imaging technique, which uses waveforms beyond first arrivals to create a detailed model of a selected physical property of the subsurface. Models produced by FWI are able to resolve subsurface physical properties to approximately half the seismic wavelength (Virieux & Operto, 2009) and can thus be used to image fine-scale geological features with a higher resolution than traditional tomographic models (for example, for rock with velocity ~2,200 m/s using our inversion strategy we would be able to recover features measuring ~140 m). FWI is often used to recover P wave velocities and has previously been successfully applied to seismic data acquired across the central Nankai subduction zone in Japan, revealing a continuous low-velocity zone that was interpreted as a potential fluid conduit associated with the megasplay fault system (Kamei et al., 2012).

Using 2-D marine seismic data along line 05CM-04 (Figure 1), recorded on a 12-km streamer, we employ FWI to obtain a high-resolution 2-D P wave velocity model of the subsurface across the north Hikurangi subduction zone. Paraxial ray tracing shows that the refracted part of the input wavefield, which FWI principally utilizes, does not travel through the subducting slab (see section 4.2), so we cannot accurately resolve velocity structure across the plate boundary fault within the area of confirmed slow slip at a depth of 2,000 mbsf (Figure 1c; Wallace et al., 2016). Here, we use FWI to image the overriding plate above the plate boundary fault, including the fault plumbing system above the zone of SSEs, and provide constraints on the fault structure, and lithological nature of incoming rocks, which may influence seismic behavior. This study also provides a framework for the future application of 3-D FWI to recently acquired, longer-offset, seismic data to recover high-resolution physical properties in zones of slow slip directly.

2. Geological Setting

The Hikurangi subduction margin is located along the east coast of the North Island, New Zealand, where the Pacific Plate is subducting obliquely below the Australian Plate at a rate between <30 and ~60 mm/year, with a rate of ~55 mm/year offshore the town of Gisborne (Barker et al., 2009; Wallace et al., 2004; Walcott, 1987; Figure 1). The margin exhibits a variety of seismic behavior, and seismic reflection and bathymetry data reveal that the northern Hikurangi margin is characterized by the subduction of seamounts and extensive splay faulting. In this section the seismic behavior of the margin and geology of the accretionary wedge and incoming sedimentary section are discussed.

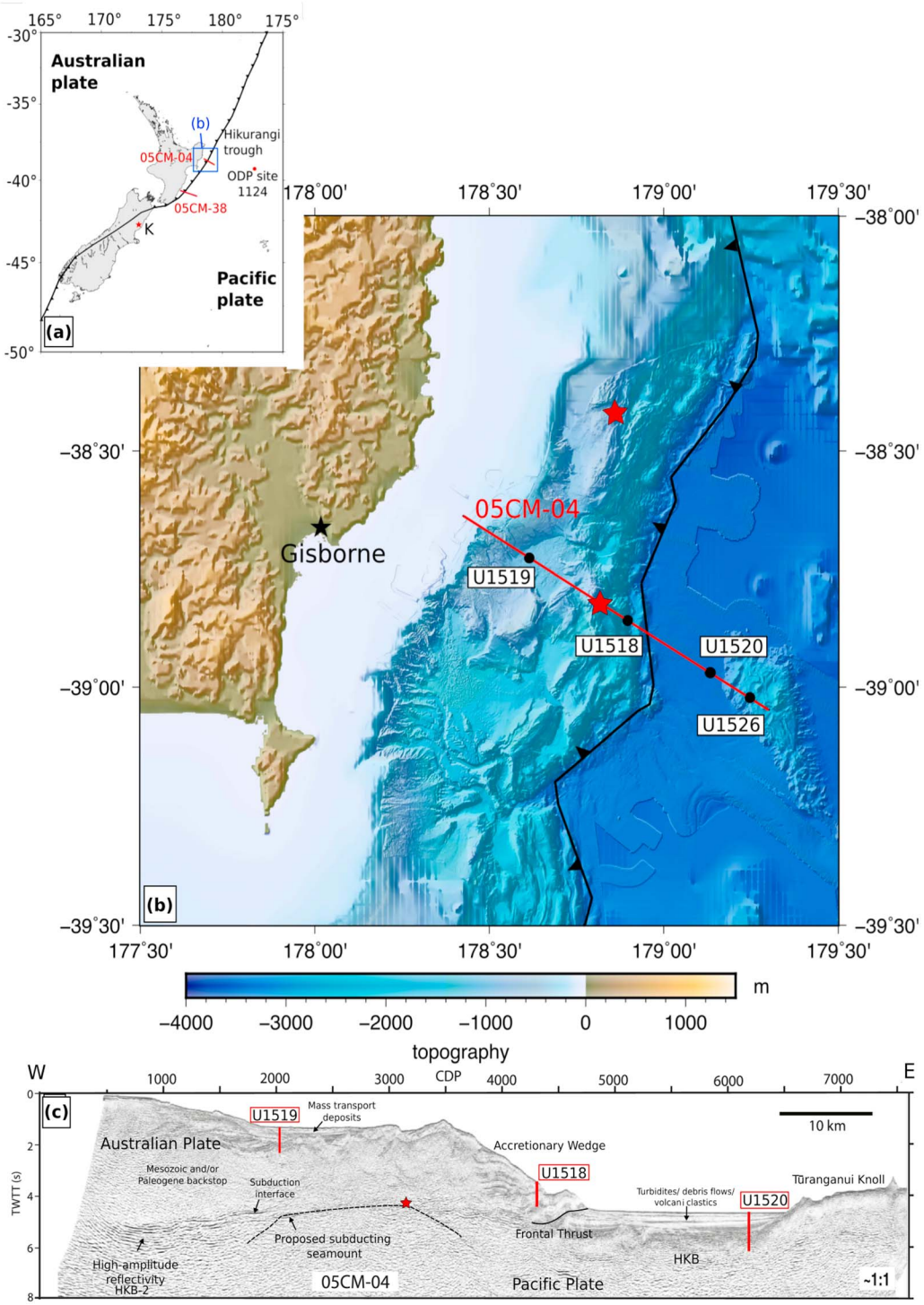

Figure 1. (a) Regional map of New Zealand showing plate boundaries. Red lines show the 2-D multichannel seismic lines 05CM-04 (used in this study) and 05CM-38 (Barker et al., 2009). The blue box shows the location of (b), the larger map, in which the color scale is offshore bathymetry across the Hikurangi margin, based on 25-m gridded swath data. The black dots represent the drill sites, where borehole velocity measurements were taken on International Ocean Discovery Program (IODP) Expedition 372 at U1519, U1518, and U1520. The red stars show the location of the 1947 Offshore Poverty Bay (along line 05CM-04) and Tolaga Bay tsunami earthquakes (Bell et al., 2014). (c) Reflection seismic section of 2-D line 05CM-04. The dashed line shows the location of the proposed subducting seamount from Bell et al. (2014) based on magnetic data, and the red star shows the location of the March 1947 tsunami earthquake event offshore Poverty Bay. The red lines represent three IODP drill sites. The different lithology types based on interpretations from the literature are shown including the Hikurangi Plateau basement sequence (HKB) and the location of the frontal thrust in the near surface, the variable reflectivity of the subduction interface, and the Tūranganui Knolls (after Bell et al., 2014).

2.1. Seismic Character of the North Hikurangi Margin and Seamount Subduction

The Hikurangi subduction plate boundary fault has experienced limited historically recorded large-scale interplate seismicity over the last 200 years. Some of the largest historically known Hikurangi plate boundary fault rupturing earthquakes occurred in March and May 1947 (Bell et al., 2014; Bell et al., 2010; Doser & Webb, 2003; Hamling et al., 2017). These earthquakes had moment magnitudes of M_w 6.9–7.1, but local magnitudes of only M_L 5.6 and 5.9, and caused abnormally large tsunami compared to other earthquakes at comparable depth and magnitude (runup heights up to 10 m; Bell et al., 2014; Downes et al., 2001); events such as these have previously been termed *tsunami earthquakes* and are inferred to have long rise times compared to other earthquakes (Kanamori, 1972). Tsunami earthquakes have been linked to regions of conditional frictional stability, possibly associated with high fluid pressures (Bell et al., 2010; Bilek & Lay, 2002; Scholz, 1998; Seno, 2002).

Geodetic data reveal that the Hikurangi margin hosts a range of SSEs. SSEs are defined as episodic events causing ~10 s of centimeters of slip over timescales of days to months, too slow to generate seismic waves yet faster than the rate of plate boundary displacement (Bartlow et al., 2014; Wallace et al., 2012; Wallace et al., 2014; Wallace et al., 2016). Continuous GPS data have shown that the Hikurangi plate boundary fault experiences both deep and shallow SSEs (Bell et al., 2010; Douglas et al., 2005; McCaffrey et al., 2008; Wallace et al., 2009; Wallace et al., 2016; Wallace & Beavan, 2006; Wallace & Beavan, 2010). SSEs at the northern margin, offshore Gisborne, are generally shallow (<2–15 km below seafloor) and occur every 18 to 24 months (Wallace et al., 2016). The updip extent of these SSEs has been poorly constrained by the land-based cGPS observations, but the recent addition of data from offshore APGs has produced direct evidence for events extending to within 2 km of the seafloor and possibly extending all the way to the trench (Wallace et al., 2016). These shallow SSEs accommodate slip equivalent to that in an earthquake with moment magnitude of ~6.3–6.8 M_w and typically result in 1–3 cm of horizontal surface displacement over 1 to 2 weeks (Wallace et al., 2004; Wallace et al., 2009; Wallace et al., 2012; Wallace et al., 2016; Wallace & Beavan, 2010). The southern part of the Hikurangi margin experiences larger (~M_w 7.0), longer-lasting (>200 days), and deeper (25–60 km depth) SSEs than in the north (Wallace et al., 2004; Wallace et al., 2009; Wallace et al., 2012; Wallace et al., 2016; Wallace & Beavan, 2010).

Seamount subduction occurs along the Hikurangi margin, with several large seamounts observed both at the seafloor of the incoming plate (e.g., Tūranganui Knoll, Figure 1) and subducted, as inferred from seismic reflection and magnetic data along the northern part of the margin (Figure 1c; Barker et al., 2018; Barker et al., 2009; Barnes et al., 2018; Barnes et al., 2010; Bell et al., 2014; Bell et al., 2010; Collot et al., 2001; Pedley et al., 2010). The subduction of seamounts has been proposed to cause extensive faulting and deformation within the upper plate (Dominguez et al., 1998; Wang & Bilek, 2014). Ocean bottom seismometers (OBSs) and APGs also resolve episodic tremor occurring after SSEs, localized in the vicinity of two subducted seamounts within and updip from areas exhibiting SSEs (Todd et al., 2018). Three areas of high-amplitude reflectivity have been identified downdip of subducted seamounts and have been interpreted as being the result of entrainment of fluid-rich sediments (Bell et al., 2010). The subduction of seamounts surrounded by trench sediment would also produce large lithology variations within the plate boundary fault zone, which may lead to variable slip mode behavior (Bell et al., 2010; Bilek et al., 2014; Saffer & Wallace, 2015; Wang & Bilek, 2014). As large amounts of unconsolidated, fluid-rich sediment are entrained by subducting seamounts, and subjected to extensive loading, increased overburden stress may lead to increased pore fluid pressures, if a low-permeability seal exists above the plate boundary fault (Ellis et al., 2015). If, however, parts of the plate boundary fault zone are permeable, these fluids, together with fluids sourced from dehydration reactions at depth, will percolate into the overriding plate and potentially also escape along splay faults if they are higher-permeability conduits than the surrounding wedge (Antriasian et al., 2018; Barnes et al., 2010; Lauer & Saffer, 2012; Saffer, 2003; Saffer & Tobin, 2011; Tobin & Saffer, 2009).

2.2. Character of the Plate Interface and Accretionary Wedge

The plate interface itself is marked by both low- and high-amplitude reflections, and in places its position is inferred from frontal thrust fault intersections (Figure 1c). Seismic reflection data reveal that several large splay faults exist within the accretionary wedge, which sole into the subduction plate boundary fault (Barker et al., 2009; Barnes et al., 2010; Barnes & Mercier de Lépinay, 1997; Ghisetti et al., 2016; Lewis & Pettinga, 1993; Mountjoy & Barnes, 2011; Plaza-Faverola et al., 2016; Plaza-Faverola et al., 2012). Splay

faults across the Hikurangi margin are primarily northwest dipping, and some have large measurable displacements within the frontal wedge (Barnes et al., 2010; Barnes et al., 2018; Ghisetti et al., 2016). Fluid flow along splay faults may be expected due to widespread active fluid seepage observed at the seafloor on the crests of thrust-related bathymetric ridges offshore of Hawke's Bay and Wairarapa (Barnes et al., 2010; Fagereng et al., 2019; Greinert et al., 2010; Plaza-Faverola et al., 2016).

Plaza-Faverola et al. (2016) conducted a PSDM along profile 05CM-38 (Figure 1a), ~220 km to the SW of line 05CM-04, and identified splay faults branching from the décollement associated with high-amplitude reflections, some with polarity reversals, indicating a decrease in acoustic impedance. Velocity analysis by Plaza-Faverola et al. (2016) resolved the depth of the subduction interface between ~7 and 14 km depth and showed reduced *P*-wave velocities below several bright, dipping reflections, which they suggest could indicate the upward flow of fluids. Plaza-Faverola et al. (2016) also note a correlation between the zone of maximum cumulative slow slip and the lowermost (~14 km) level of splay faulting and posit that the presence of overpressured fluid-rich sediment could be related to mechanisms of slow slip. Faults observed in seismic data offshore Gisborne are mostly defined by stratigraphic cutoffs rather than fault plane reflections (e.g., Figure 1c; Barker et al., 2018; Barker et al., 2009; Bell et al., 2010), so we cannot use reflection polarity to interpret whether the faults are low acoustic impedance zones here or not. While several instances of fluid seeps have been identified in the region, typically in 700–1,200 m water depth on the crests of thrust faults in the midslope, it is yet undetermined whether the faults identified along like 05CM- 04 are conduits or seals. As the role of fluids at subduction zones may play a key role in determining the seismicity of the interface (Bangs et al., 2014; Bangs et al., 1999; Saffer & Wallace, 2015; Tobin & Saffer, 2009), one of the key aims of this study is to determine whether faults offshore Gisborne may be high-porosity, high-permeability fluid conduits.

2.3. Incoming Sedimentary Section

The lithology of the material that forms the incoming subducting plate is important, as the plate boundary fault will form somewhere within it when it reaches the deformation front. Lithologies across the margin were previously not well known due to a lack of drilling data, and interpretation of the stratigraphy up until now has been based on comparisons between reflection seismic data and ODP borehole data (Leg 181, wells 1123 and 1124) from east of the trench (Davy et al., 2008). New IODP drilling data (Expeditions 372 and 375) collected in 2017/2018 will provide a much improved understanding of stratigraphy (Pecher et al., 2019; Wallace et al., 2019).

Reports from IODP Expedition 372 and 375 site U1520 have determined six lithostratigraphic units in the incoming section, consisting of turbidites, mass transport deposits, and hemipelagic muds down to 509.82 mbsf, pelagic carbonate facies from 509.82 to 848.45 mbsf, volcaniclastics from 848.45 to 1016.24 mbsf, and a blend of volcaniclastics, mudstone, limestone, and siltstone down to 1,045.75 mbsf (Wallace et al., 2019). Based on the seismic reflection character, the seaward part of the accretionary wedge is likely to be largely composed of accreted turbidites and pelagic sediments (e.g., Barnes et al., 2017; Fagereng et al., 2019; Ghisetti et al., 2016). The subducting plate (Hikurangi Plateau) is an ~10-km-thick, buoyant Large Igneous Province that includes large seamounts and other volcanic features (Carter et al., 2002; Davy et al., 2008; Davy & Wood, 1994; Hoernle et al., 2010). The upper seismic sequence (HKB, Figure 1c) has been interpreted as reflective volcaniclastics and other Cretaceous sedimentary rocks (Wallace et al., 2019). Based on seismic and magnetic data (Barker et al., 2018; Davy et al., 2008), the underlying plateau basement is thought to comprise a higher velocity igneous layer.

3. Data Sets

Figure 1 shows the location of the 2-D marine seismic profile used in this study, acquired in May 2005 as part of the 05CM survey (Barker et al., 2009; Multiwave, 2005). Line 05CM-04 is 90 km long and was collected by Multiwave Geophysical aboard the MV Pacific Titan, using a 12-km-long streamer with 960 channels spaced 12.5 m apart. Data were recorded to 12s two-way traveltime (TWT) and with a shot spacing of 37.5 m. The reflection seismic section is shown in Figure 1c (Bell et al., 2014), PSDM velocity image of profile 05CM-04 is shown in Figure 4a (Barker et al., 2018), and two example shot gathers from this data set are shown in Figure 4b and 4c.

In 2017–2018 IODP drilled four sites along line 05CM-04 (Figure 1) during Expeditions 372 and 375 (Pecher et al., 2019; Wallace et al., 2019). These expeditions collected LWD, wireline (U1520 only), and core data within the accretionary prism and trench (Figure 1c). In this study sonic logs recorded in these expeditions will be compared with our FWI velocity models. LWD sonic data were recorded to a depth of 590.4 mbsf in U1519, 564.9 mbsf in U1518, and 714.6 mbsf in U1520. In U1520 open hole wireline sonic logs were also recorded down to 947 mbsf.

4. Method and Data Analysis

We use FWI as it has the potential to produce high-resolution models of any physical property that influences the seismic wavefield (Pratt, 1999; Sirgue et al., 2010; Tarantola, 1984; Virieux & Operto, 2009; Warner et al., 2013). In practice, in most commercial applications, a robust model of *P* wave velocity is recovered using three-dimensional acoustic, anisotropic FWI codes (Sirgue & Pratt, 2004; Warner et al., 2013). Although accurate modeling of the seismic wavefield requires a three-dimensional elastic code that can account for changes in *S* wave velocity, anisotropy, density, and attenuation, this is normally prohibitively computationally expensive. In addition, the amplitudes of individual arrivals are sensitive to several physical properties, so multiparameter inversions tend to be less robust due to cross talk between individual parameters (Sirgue & Pratt, 2004; Virieux & Operto, 2009). In the inversions shown here, we have normalized amplitudes between different time slices using stabilized amplitude matching that varies smoothly and slowly in both space and time independently for both observed and predicted data, and we have balanced trace amplitudes between predicted and observed data using a scheme that is sensitive to the similarity between the two data sets, and that is also stabilized and varies smoothly in space (Warner et al., 2013). This largely, but not completely, mitigates for amplitude changes that are related to attenuation, density, elasticity, and short-wavelength changes in anisotropy, while largely, but not completely, retaining those amplitude affects that are related directly to the *P* wave velocity model. Apart from applications focused on imaging the reservoir and drilling hazards in petroleum exploration, FWI has also been used to resolve the *P* wave velocity structure of crustal-scale targets in a range of tectonic settings, including subduction zones (Calvert et al., 2011; Christeson et al., 2012; Kamei et al., 2012; Morgan et al., 2011).

Here we use a 2-D version of the 3-D Imperial College time-domain code (Warner et al., 2013). The code uses both velocity and density contrasts to produce reflections, and the two models are coupled together using Gardner's law to estimate density from *Vp*. We utilize the acoustic approximation of the wavefield, since there are no a priori constraints on anisotropy, *S* wave velocity, attenuation, or density. Given this approximation, we can expect there to be some inaccuracies in the recovered *P* wave model; for example, if anisotropy is not accounted for, FWI velocity models are stretched and the depths inaccurate. This was observed in the recent drilling of the Chicxulub impact crater, where FWI-determined (subhorizontal) velocities obtained prior to drilling (Morgan et al., 2011) led to an overestimate in the vertical velocity within the sedimentary overburden and corresponding depth to the crater (Christeson et al., 2018).

In FWI a source wavelet is propagated through a starting *P* wave velocity model, $\mathbf{m}$, to obtain a predicted seismic data set, $\mathbf{p}$:

$$\mathbf{G}(\mathbf{m}) = \mathbf{p} \tag{1}$$

where $\mathbf{G}$ describes a function, which calculates the seismic data given the model. A residual data set is calculated by taking the difference between $\mathbf{p}$ and the acquired field data set $\mathbf{d}$, and this residual data set is then back-propagated through the model. A cross correlation between the forward and back-propagated wavefields is computed in time at every point in the model, $\mathbf{m}$, to produce a gradient for each source. Stacking these gradients together produces a global gradient, which is used to update the model, $\mathbf{m}$. These steps are repeated, and the starting velocity model is iteratively updated via a sequence of linearized local inversions to solve the equation:

$$\mathbf{G}^{-1}(\mathbf{d}) = \mathbf{m}' \tag{2}$$

where $\mathbf{m}'$ is the final model of the subsurface at the point when the misfit, or the sum of the squares of the residual data set, is minimized, and model updates become small (Asnaashari et al., 2013; Tarantola, 1984; Warner et al., 2013).

The FWI workflow adopted here follows Warner et al. (2013) and involves the following steps, which will be discussed in more detail below:

1. The data set was preprocessed in preparation for FWI.
2. A source wavelet was generated.
3. A starting velocity model was selected.
4. The adequacy of the source wavelet and starting velocity model were quality checked by comparing the observed and predicted data.
5. Inversion strategies were tested and an inversion scheme selected.
6. The data set was inverted using the selected inversion scheme, with regular quality assurance to check for cycleskipping.

Steps 4 and 5 are particularly important in order to avoid cycleskipping in the inversion (Asnaashari et al., 2013; Pratt, 1999; Tarantola, 1984; Warner et al., 2013). Cycleskipping occurs when arrivals within the synthetic and real data sets differ by more than half a cycle, causing the velocity model to converge to a local rather than global minimum (Sirgue et al., 2010; Tarantola, 1984; Virieux & Operto, 2009). Ideally, to mitigate this problem, FWI should start at low frequencies, since the traveltimes are easier to match within half a cycle for larger periods. The inclusion of lower frequency data in the inversions leads to improvement in the long-wavelength velocity structure, and the maximum frequency of the input data can then be gradually increased to introduce the finer-scale structure. As frequencies are increased, however, so too do computational costs due to the necessity of finer grids and smaller time steps, so frequencies need to be selected carefully based on the minimum and maximum subsurface velocity structures (Delescluse et al., 2011; Pratt, 1999; Tarantola, 1984; Virieux & Operto, 2009; Warner et al., 2013).

4.1. Implementing the Workflow

4.1.1. The data Set Was Preprocessed in Preparation for FWI

As noted above, FWI is more likely to be successful when the input data include low-frequency signal. The 2-D seismic line used in this study, however, was contaminated with swell noise, as shown in the raw shot gather (Figure 2a). As a result of this noise, the lowest useable frequency was determined to be ~3 Hz. A small amount of preprocessing was undertaken to prepare the data for input to FWI. This consisted of F-K filtering to remove tailbuoy noise and band-pass filtering to limit data to frequencies between 3 and 8 Hz (Figure 2b). An additional F-X deconvolution was applied to further reduce swell noise, and this produced a much cleaner dataset (Figure 2c). This was applied to all data (see further examples of filtered data in Figures 4b and 4c).

4.1.2. Generate a Source Wavelet

A predicted data set, $\mathbf{p_1}$, is obtained by propagating an initial source wavelet, $\mathbf{w_1}$, through the starting model. We wish to find a filter, $\mathbf{f}$:

$$\mathbf{p_1}{}^{*}\mathbf{f}\approx\mathbf{d} \tag{3}$$

where $\mathbf{d}$ is the field data.

Here, the initial estimate of the source wavelet, $\mathbf{w_1}$, is a spike that has been filtered using the same filters that were applied to the field data (Figure 2a). This source wavelet is then propagated though the water column to generate a direct water wave arrival on the streamer (Figure 3b, left hand trace). The filter, $\mathbf{f}$, is then determined by solving the equation:

$$\mathbf{p_1}{}^{*}\mathbf{f}\approx\mathbf{d}\Rightarrow\mathbf{p_1^{-1}}{}^{*}\mathbf{d} \tag{4}$$

For which $\mathbf{d}$ is the observed data at the same location as the predicted (Figure 3b).

We then compute

$$\boldsymbol{w_1}{}^{*}\boldsymbol{f}=\boldsymbol{w_2} \tag{5}$$

where $\boldsymbol{w_2}$ is the new source (Figure 3c) and then $\mathbf{w_2}$ is used to generate the new predicted data, $\mathbf{p_2}$, such that

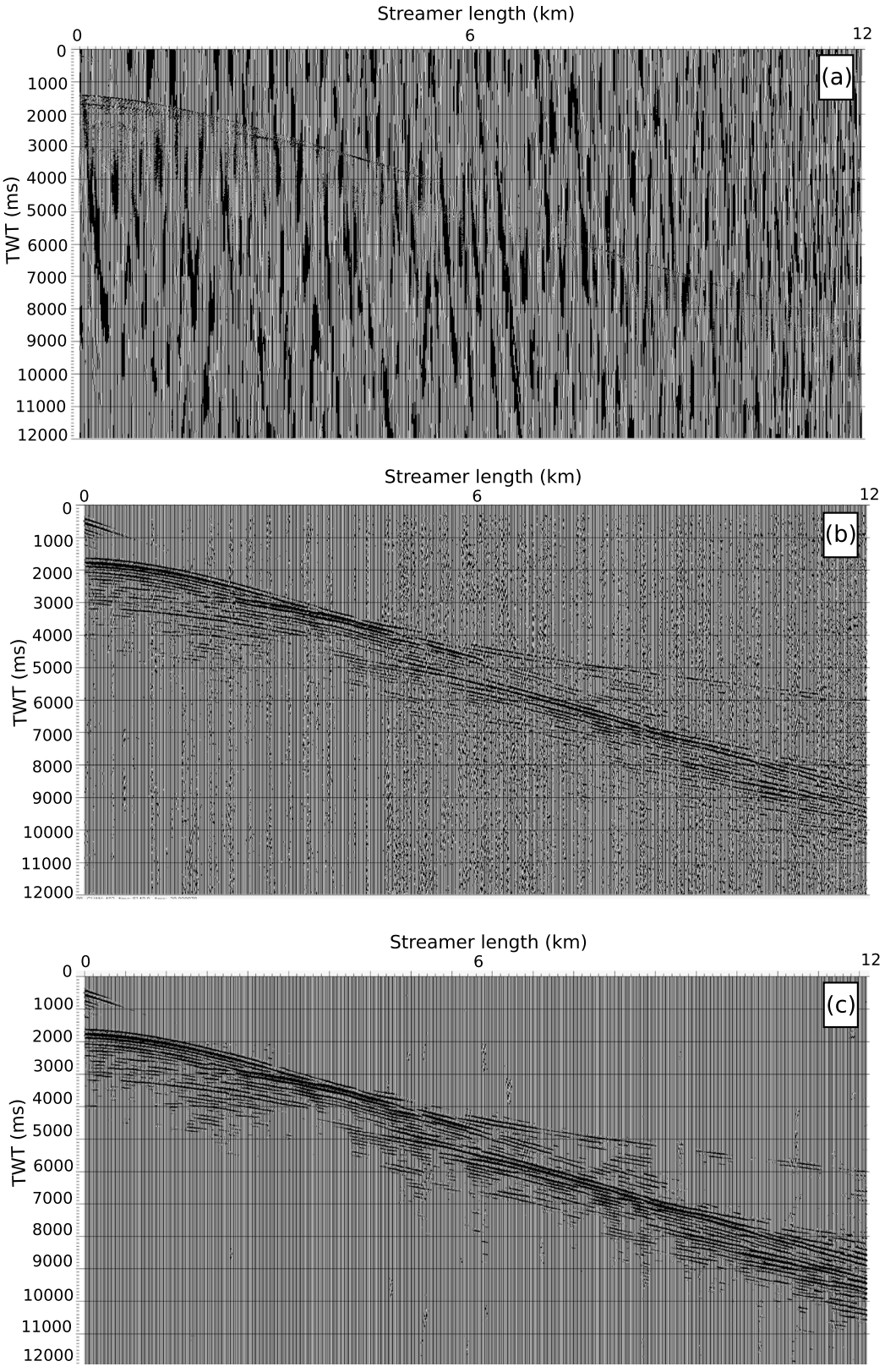

Figure 2. (a) Raw shot gather; the data are dominated by swell noise. (b) The same shot gather after band-pass and F-K filters have been applied to remove swell noise. The shot gather is much cleaner; however, there is still a large amount of random noise across the gather. (c) The same shot gather after the application of F-X deconvolution to the gather shown in (b). While the data still contain some noisy traces, the majority of swell noise has been removed.

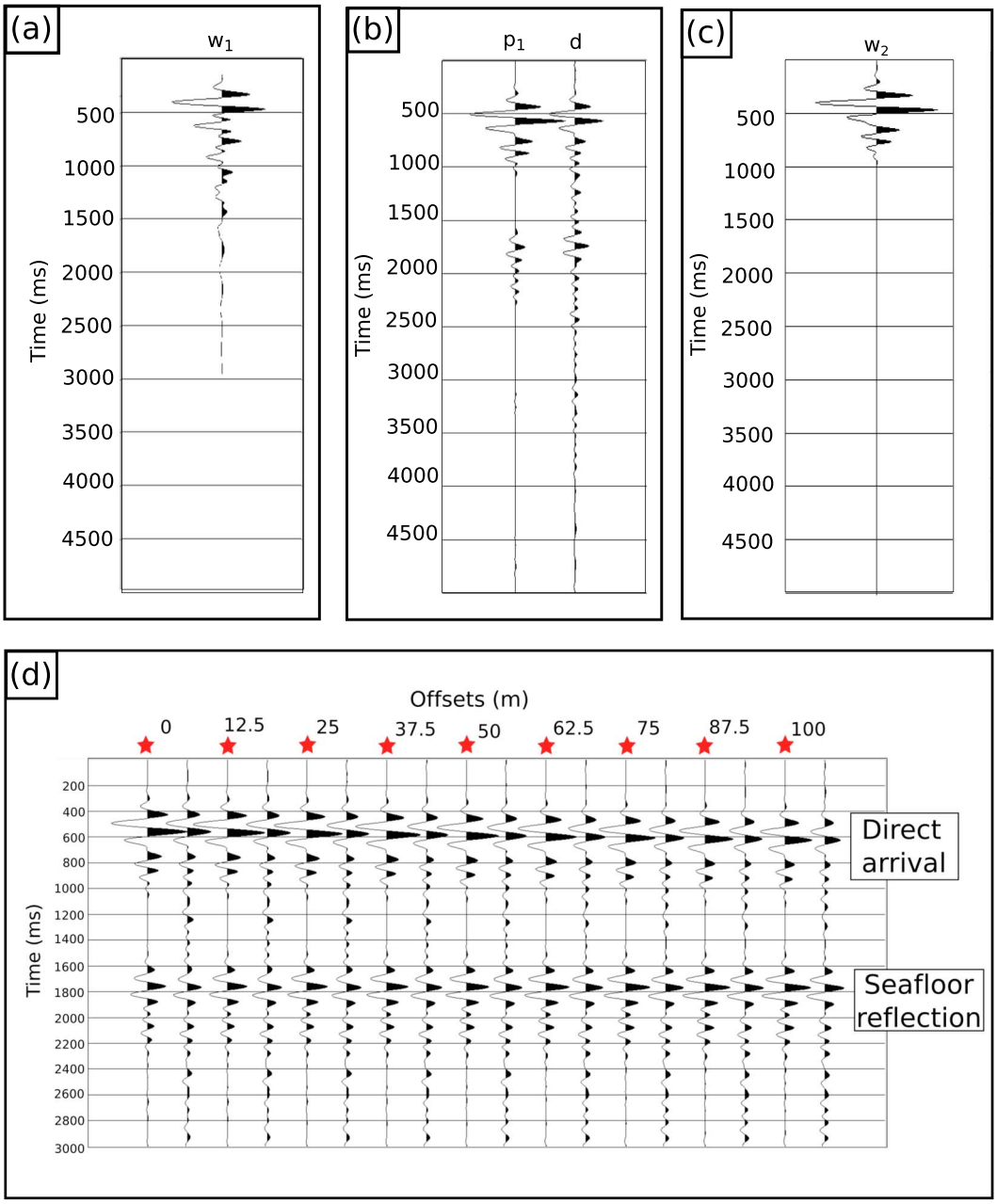

Figure 3. (a) The original source wavelet $\boldsymbol{w_1}$, a band-pass filtered spike (b) The predicted data$\boldsymbol{p_1}$ on the left, and the same trace from the field data $\boldsymbol{d}$ on the right. (c) The final source wavelet $\boldsymbol{w_2}$ after application of the matching filter $\boldsymbol{f}$ to $\boldsymbol{w_1}$. (d) Side-by-side comparison of the predicted, $\boldsymbol{p_2}$ (indicated by a red star), and observed data, $\boldsymbol{d}$, for a single shot gather of the 2-D seismic data used in this study.

$$\boldsymbol{p_2} \approx \mathbf{d} \tag{6}$$

By comparing the predicted data, $\mathbf{p_2}$, with the observed, $\mathbf{d}$, we can assess the accuracy of the new wavelet $\mathbf{w_2}$. Figure 3d shows a side-by-side comparison of nine traces from a single shot gather with the synthetic data produced using $\mathbf{w_2}$ interleaved with the same nine traces from the field data, up to offsets of 272.5 m from the start of the streamer. We can see that the traveltimes of the main peaks and troughs in the arriving waveforms match well for both the direct water wave arrival between 200 and 1,000 ms and the seafloor reflection, between 1,600- and 2,200 ms time. The principal difference between traces is the presence of noise within the observed data.

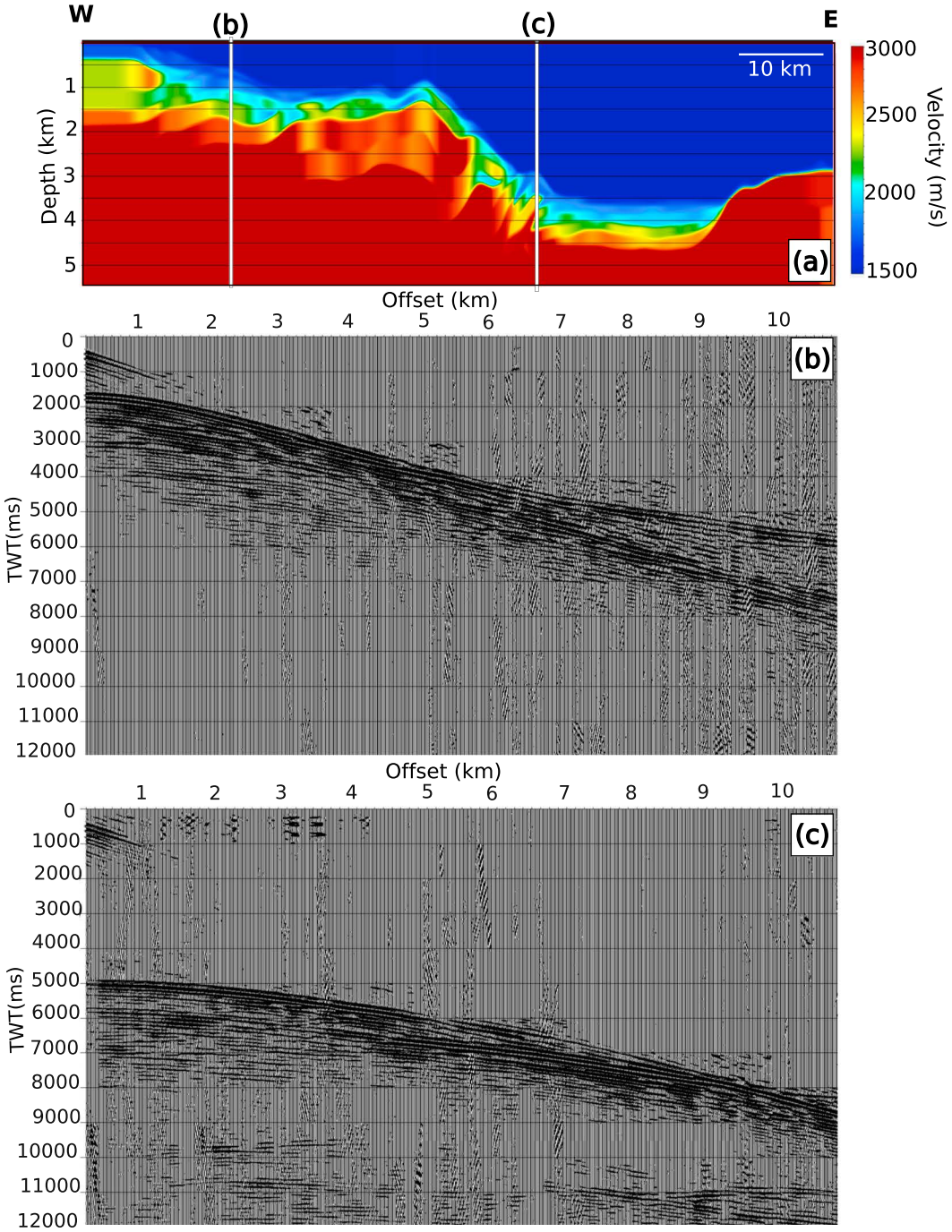

Figure 4. (a) Prestack depth migration (PSDM) velocity model by Barker et al. (2018). Panels (b) and (c) show filtered shot gathers at the two points labeled on the model.

4.1.3. Selecting a Starting Velocity Model

An initial velocity model was provided by Barker et al. (2018; Figure 4a), which was created for a PSDM of the seismic data using Paradigm's Geodepth. Prestack time migration velocities and a geological model were used to construct an interval velocity model as a function of depth, which was then iteratively refined through residual velocity analysis and inspection of the PSDM stack and gathers. While this is an effective way to produce a velocity model for reflection imaging (Yilmaz, 2001), the method is dependent on Normal Move-Out, which is relatively insensitive to velocity, as a range of subsurface velocity structures

can be used to stack the same reflections successfully. Prior to use as a starting model for FWI, several changes were made to the PSDM velocity model presented in Barker et al. (2018). First, water velocities that were collected using Expendable Bathythermographs (XBTs) in the area from the National Oceanic and Atmospheric Administration (NOAA) were used to construct the velocity in the water column. Then the seafloor was modified to match the bathymetric data collected in the area (Figure 1). Selecting the water velocities and seafloor depths is an important factor in completing successful inversions using FWI, so much care was taken in selecting these. Extensive testing of different seafloor depths and ocean velocities using techniques such as Normal Move-Out analysis and short-offset receiver gathers and careful determination of how these affected synthetic gathers lead to the final selection of appropriate values for both the seafloor and ocean velocities. Finally, rock velocities below the seabed were smoothed to remove all abrupt changes below the seafloor except the seabed itself, as FWI is more efficient if only well-constrained boundaries are placed in initial starting models (Morgan et al., 2016). The modified starting velocity model that is used for FWI in this study is shown in Figure 5a.

4.1.4. The Adequacy of the Source Wavelet and Starting Velocity Model

The quality of the source wavelet and starting model was investigated by directly comparing predicted seismic data acquired through the model with the field data. The starting model will generate matching waveforms for the direct arrival into the streamer and seafloor reflection if the model for the ocean velocity and seafloor depth is reasonably accurate. We also examined later arrivals and longer-offset refractions to check whether they are cycleskipped, and we use this information to determine which data should be input into the initial inversions. Figures 4b and 4c show the field data for two shot gathers, whose locations are indicated on the model in Figure 4a. Figures 5b–5g show the interleaved predicted and field data, with 10 traces of synthetic data followed by 10 traces of real data. The synthetic data are shown with a pink overlay.

From Figure 5 we can see that there is a good match between real and synthetic waveforms for both the direct arrival and the seafloor reflection out to about 5 km offset. We can also see that the waveforms align well for the first seabed multiple (at ~3,000 ms for shot gather B and ~10,000 ms for C). The match is shown in greater detail in boxes d and f. Boxes d and f both show a continuous reflection across both the real and synthetic data for the direct arrival and seafloor reflection. Boxes e and g, however, highlight the mismatch between the real and synthetic data at longer offsets, as the reflections in the field data and the synthetic data do not align. This match is typical for shot gathers across the margin. This indicates that the seafloor and water velocities are reasonably accurate and suitable for use in FWI. The match at greater times and offsets is poorer, as expected, but some seismic phases are seen to match within half a cycle (Figures 5d and 5f). This indicates that we have selected an appropriate starting velocity model and that we can use these comparisons to remove any clearly cycle-skipped data from the inversions. For example, some of the reflections at long offsets appear to be over half a cycle out of phase with the real data (Figures 5e and 5g). In our adopted inversion scheme cycle-skipped data are excluded from the initial inversions, and more data are added as the match improves to be less than a half-cycle out of phase.

4.1.5. Inversion Strategies Were Tested and an Inversion Scheme Selected

A good inversion strategy is important to ensure that the majority of the input data are not cycleskipped and the models are slowly improved, with the misfit function converging to a global rather than a local minimum. Several different inversion tests were undertaken, including using different time windows, frequency windows, and offsets. One of the main issues with FWI is that its specific application is highly dependent on the data set, and so no individual inversion strategy works for all data sets. Exhaustive testing of this data set revealed the most effective inversion scheme as outlined below. The chosen inversion scheme is as follows:

A 2s window was applied to the data using mutes to remove the direct water wave, noise above the first arrivals from the seafloor and later arriving multiples and possible *S* waves. Multiples are still present in this window but are included as testing has shown that including multiples and ghosts in the FWI inversion produces reliable and stable results (Warner et al., 2013). The data were inverted in eight frequency blocks, for which the input data are band-passed using minimum-phase Ormsby filters with 0.1% noise and 1Hz roll-off to remove frequencies higher than a maximum frequency, set to values from 3 to 8 Hz, with 20 iterations for each frequency block (Table 1). Frequencies, time sampling, and grid size are dependent on each other as the code requires the wavefield to cross <0.5 grid points per time step. Velocities within the water column, and the location of the seabed, were kept fixed during the inversion. At these inversion frequencies (up to 8 Hz) we can theoretically resolve spatial features ranging from ~100 m in size at the lowest velocities in the model

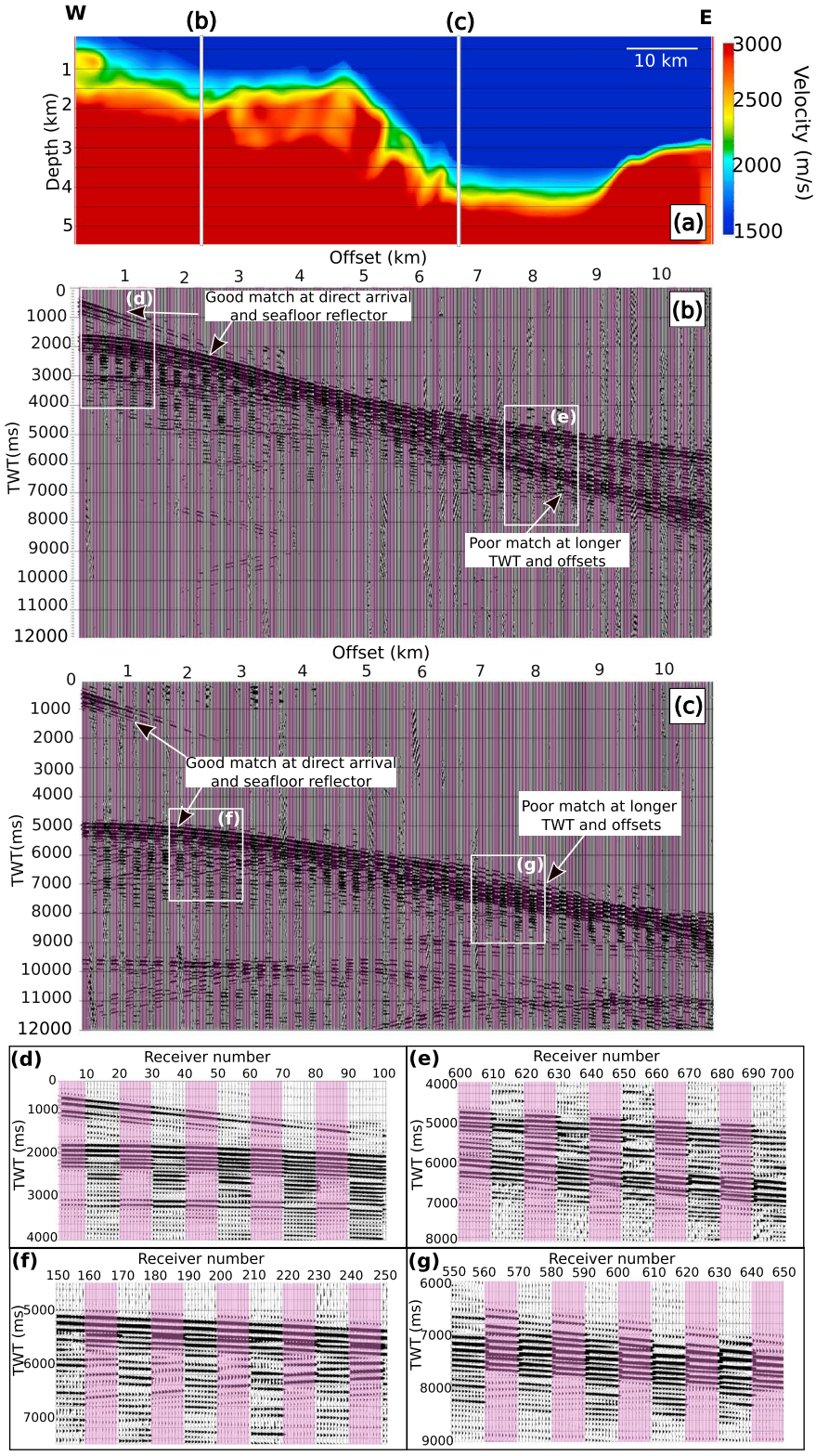

Figure 5. (a) Plot of the smoothed PSDM model from Barker et al. (2018) used here as the starting model for full-waveform inversion (FWI). (b) and (c) show the same two shots gathers as in Figure 6, with synthetic data generated using the starting model (highlighted in pink) interleaved with the observed data. The figure shows a good match for both the direct water wave arrivals and seafloor reflections and a reasonable match for some later arrivals and longer-offset refractions. (d), (e), (f), and (g) show zoomed in plots of data from within the boxes shown in (b) and (c). From these more detailed views, we can see that some of the later arrivals and longer offset data are not well matched and may be cycle skipped.

Table 1
Parameters Used in FWI of the Data Set

Inversion type	Time-domain, isotropic
Total number of sources	2,173
Shot spacing (m)	37.5
Maximum number of streamer receivers per composite source	Up to 870
Receiver spacing (m)	12.5
Offset between shot and first receiver (m)	160
Grid size (m)	12.5
Time sampling interval (ms)	1
Maximum frequency in each frequency block	3.0, 3.4, 3.9, 4.5, 5.2, 6.0, 7.0, 8.0
Iterations per frequency	20

of ~1,520 m/s to ~200 m at greater depth where velocities increase to ~3,200 m/s. Each shot was used twice in each iteration block of 20 iterations per frequency, with each iteration using every tenth shot.

Starting with a default number of iterations per frequency, based on previous applications of the code, the data set is inverted and the misfit is checked to ensure that the reduction of the misfit has become minimal. Additional tests are run if this is not the case. If step lengths become very small, the inversion has converged at that frequency, and typically, we would then move to higher frequencies. The inversions are run on a cluster of multicore CPU nodes and take between 3 and 4 days to complete using 25 nodes, which each have eight cores. The inversions were performed using these parameters and repeated three times, starting with offsets up to 6 km (481 streamer receivers per composite shot), then increasing to offset of 7.2 km (576 streamer receivers per composite shot), and finally up to 10.87 km (870 streamer receivers per composite shot). After each inversion block, before adding in longer offsets, the model was smoothed in slowness via a 2-D convolutional filter measuring 60 traces horizontally and 60 time samples vertically.

While we have chosen a time-domain acoustic inversion, we are aware that attenuation can produce phase effects. These effects can be important in industrial settings where anisotropy is well constrained and exact depths are important; however, with the 05CM-04 data set, properly accounting for the dispersive effects of attenuation over the limited bandwidth that we use for FWI will not produce any substantial changes to the model other than minor shifts in absolute depths. These shifts are likely to be similar or smaller in magnitude to those produced by anisotropy, which we also have not constrained here.

4.1.6. The Data Set Was Inverted Using the Selected Inversion Scheme, With Regular Quality Assurance to Check for CycleSkipping

After computing velocity models using the inversion scheme outlined in Step 6, the models were checked after each increase in offset using the technique outlined in Step 4. This was to ensure that the time differences between arrivals in the field and synthetic data were decreasing, and the synthetic reflections and refractions were aligning with the observed data and not cycleskipped. The performance of the inversions was monitored throughout by regularly comparing the predicted and observed data, to ensure the velocity model was being updated in the right direction. Once it was ensured that the inversions were performing as desired, the final *P* wave FWI model was obtained after 160 iterations and will be discussed in section 5.

4.2. Raytracing Was Computed to Determine Maximum Target Depths

As FWI primarily uses transmitted energy in the form of postcritical, horizontally propagating refracted waves and diving waves that allow for better illumination of subsurface velocities (Warner et al., 2010), paraxial ray tracing was computed through a smoothed version of the starting velocity model (Barker et al., 2018; Stockwell & Cohen, 2002). This was carried out to determine the depths of turning rays recorded by the 12 km streamer. Results of the ray tracing show good coverage of the subsurface by seismic waves in the uppermost 1.5–2 km of the subseafloor, with some rays penetrating down to ~3.5 km depth (Figure 6). This indicates that we can expect to recover subsurface *P* wave velocities up to ~2,000 mbsf, but not from within the subducting slab and not from within the known source area of SSEs at depths of >4,000 mbsf. We also do not expect to image the igneous basement of the Hikurangi Plateau (Figure 1). Wider offset data collection is required to image to these deeper depths.

5. Results

The final *P* wave velocity model recovered with the FWI workflow discussed above is shown in Figure 7a. Compared to the PSDM velocity model by Barker et al. (2018), which has a layered, blocky appearance (Figure 4a), FWI has introduced fine-scale structure within the upper subseabed section, which appears to be geologically plausible. Close to the edge of the profile up to ~5 km from the model boundaries, and in the deeper parts (>2,000 mbsf) of the model, there are curved (raypath-like) velocity anomalies. These are typical artifacts in areas of poor wavefield coverage and can also be produced by cycleskipping. Hence,

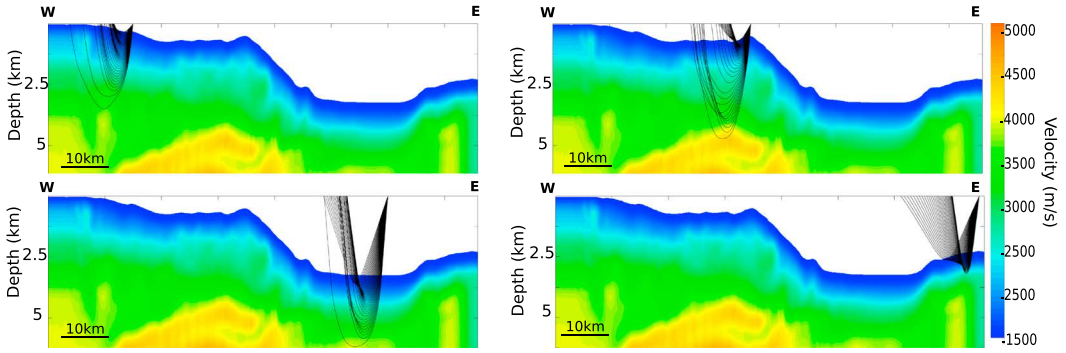

Figure 6. Paraxial ray tracing through the starting model at four locations along the line. The black lines show the rays being recorded by the 12 km-long streamer. There is good ray coverage in the uppermost 1.5–2 km of the subseafloor, with some rays penetrating down to ~3.5-km depth.

below, we focus our discussion on the parts of the velocity model that are likely to be well constrained, indicated by the white dashed line in Figure 7.

5.1. Quality Assurance

5.1.1. Comparison With the PSDM Seismic Reflection Image

To investigate whether the recovered velocity anomalies correlate with geological features observed in the PSDM seismic reflection image, we compare them in Figure 7b. We note that the PSDM reflection stack was processed with a different velocity model (the unsmoothed starting velocity model in Figure 4a), so we do not expect perfect alignment between reflections and changes in the FWI velocity model. The velocity model will be smoother than the reflection section because the former contains wavelengths corresponding only to frequencies up to 8 Hz, while the latter is at full bandwidth. In addition, the reflection section

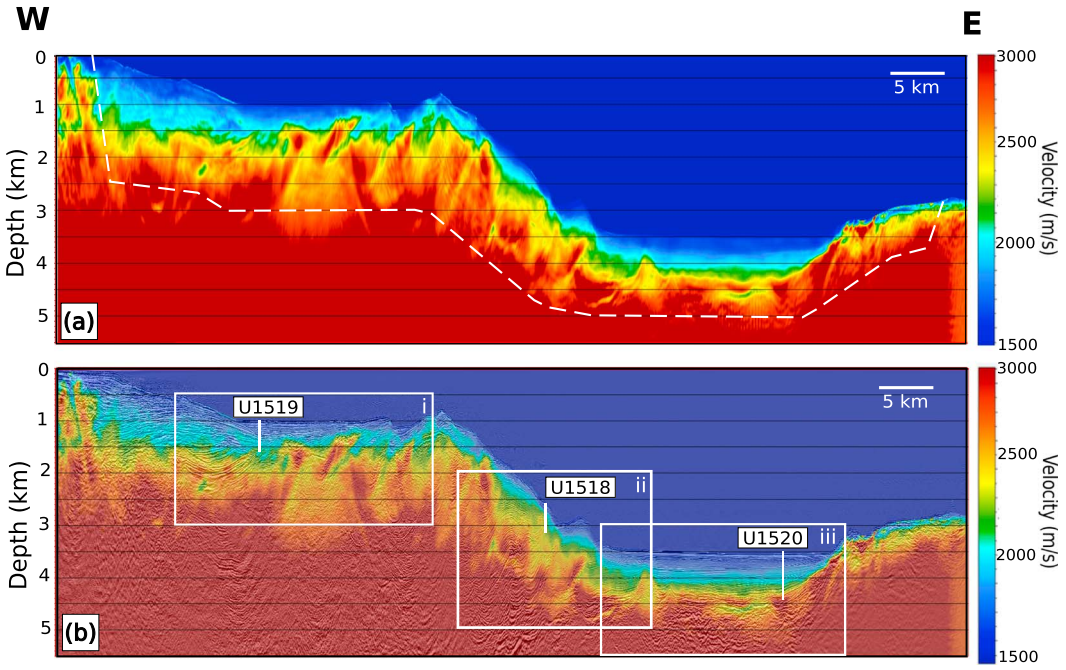

Figure 7. (a) Final *P* wave velocity model recovered after 160 iterations of FWI. The white dashed line indicates the extent of the model that we consider to be reasonably well constrained: The area below this line is likely to suffer from poor wavefield coverage. (b) Final *P* wave FWI velocity model overlain on the PSDM seismic image from Barker et al. (2018). Three areas of interest, i, ii, and ii, have been highlighted for discussion in the text. Thin white vertical lines show the location of three drill holes (U1519, U1518, and U1520) where LWD and wireline (U1520 only) data were collected during IODP Expeditions 372 and 375 (Pecher et al., 2019; Wallace et al., 2019).

represents the vertical differential of the perfect velocity model, and differentiation enhances the shorter wavelengths so that reflections sections are always rougher/sharper than their corresponding velocity models even when their nominal bandwidths are the same. Finally, as the FWI is isotropic (Table 1), any anisotropy in the subsurface will not be accounted for, which means that we also expect to see an offset in depth between individual reflections, which are more sensitive to changes in vertical velocity, and the velocity anomalies recovered by FWI, which are more sensitive to the horizontal velocity structure (Bentham et al., 2018; Christeson et al., 2018). All of these points mean that we expect the dips and depths of reflectors in the PSDM, to be slightly offset and more smoothed in the FWI velocity model. Figure 7b shows that features in the velocity model often do correlate quite closely with features that can be interpreted from the reflection image. For example, many abrupt velocity changes align with high-amplitude reflections in the seismic section. To investigate the relationship between the two models further, we have selected three areas of particular interest labeled i, ii, and iii in Figure 7b, which will be discussed in section 5.2.

5.1.2. Comparison of Real Data With Synthetic Shot Gathers

As outlined in section 4, the final step (Step 7) in the development of a FWI velocity model is to determine the fit of the model by comparing synthetic waveforms produced by propagating the source wavelet (Figure 3c), through the final *P* wave velocity model (Figure 5a), with the real field data (e.g., Figures 2c, 4b, and 4c). In Figure 5 we saw that the match between synthetic data and field data was good for the direct arrival and seafloor reflection. In Figure 8 we see comparisons between the synthetic data generated using the final model at the same points b and c shown in Figures 4 and 5, with 10 traces of the real seismic data interleaved with 10 traces of synthetic data through the final model, highlighted in pink. We see in both shot locations, the two data sets match well at longer streamer offsets and later traveltimes compared to the starting model, no longer just for the seafloor reflection. The synthetic and observed traces for many subcritical reflections and refractions are now aligned, notably, in boxes d, e, f, and g, which show zoom-ins of the shot gathers shown in b and c. By comparing Figures 5e and 5g with Figures 8e and 8g, a significant improvement to the match of the reflections across the two data sets can be seen. Comparisons show that most of the data are no longer shifted by over half a cycle; instead, we can follow the data across continuous reflections, and this is true for shot gathers across the entire model. The comparison of Figures 8 and 5 reveals that the final FWI model provides a better fit to the real seismic data than the smoothed starting model. The overall improvement in fit between the observed and synthetic waveforms suggests that the recovered FWI velocity structure is real.

5.1.3. Comparison With LWD and Wireline Sonic Logs

LWD and wireline sonic *P* wave velocity data are available along seismic line 05CM-04 from three drill sites U1519, U1518, and U1520 (Figure 1). The LWD and wireline tools sample the <1,000 mbsf every 0.5 ft (0.124 m), and the results were compared to the *P* wave velocities predicted by the starting model (Figure 5a; and the final FWI model, Figure 7a).

In general, at all three locations, the final FWI model shows an improvement over the smoothed starting velocity model, with the velocities predicted by FWI showing a closer match to the average velocities and incorporation some velocity variations recorded in the LWD and wireline data (Figure 9). An exception is in the shallow part of site U1518 where the final model is not as close to the well data as the starting model until ~180 mbsf. We take an envelope of velocities from the models, spanning 100 m either side of each drill site. At site U1519, the predicted velocities from the final FWI model match well on average throughout the logged section, however slightly underestimates the velocities between ~50 and 300 mbsf (Figure 9a). The final FWI model also detects a velocity inversion shown by the logs at a depth of ~580 mbsf, which is not shown in the starting model, but does not detect the small velocity inversion between ~330 and 340 mbsf nor at ~500–510 mbsf. At site U1518, the final FWI model underestimates velocities down to ~320 mbsf and then overestimates velocities below this (Figure 9b). Compared to the starting model, however, the final FWI model captures the velocity inversion at ~300 mbsf and follows the general trend of the velocities from the log much better than the starting model. At site U1520 the final FWI model slightly underestimates velocities between 100 and 220 mbsf and slightly overestimates velocities from ~220 to 500 mbsf, however matches the velocity trend well (Figure 9c). The predicted velocities from the final FWI model show a good match from ~500 to 850 mbsf. The velocity inversions detected by the *Vp* log at ~850 and ~900 mbsf are present in the final FWI model but are not as pronounced.

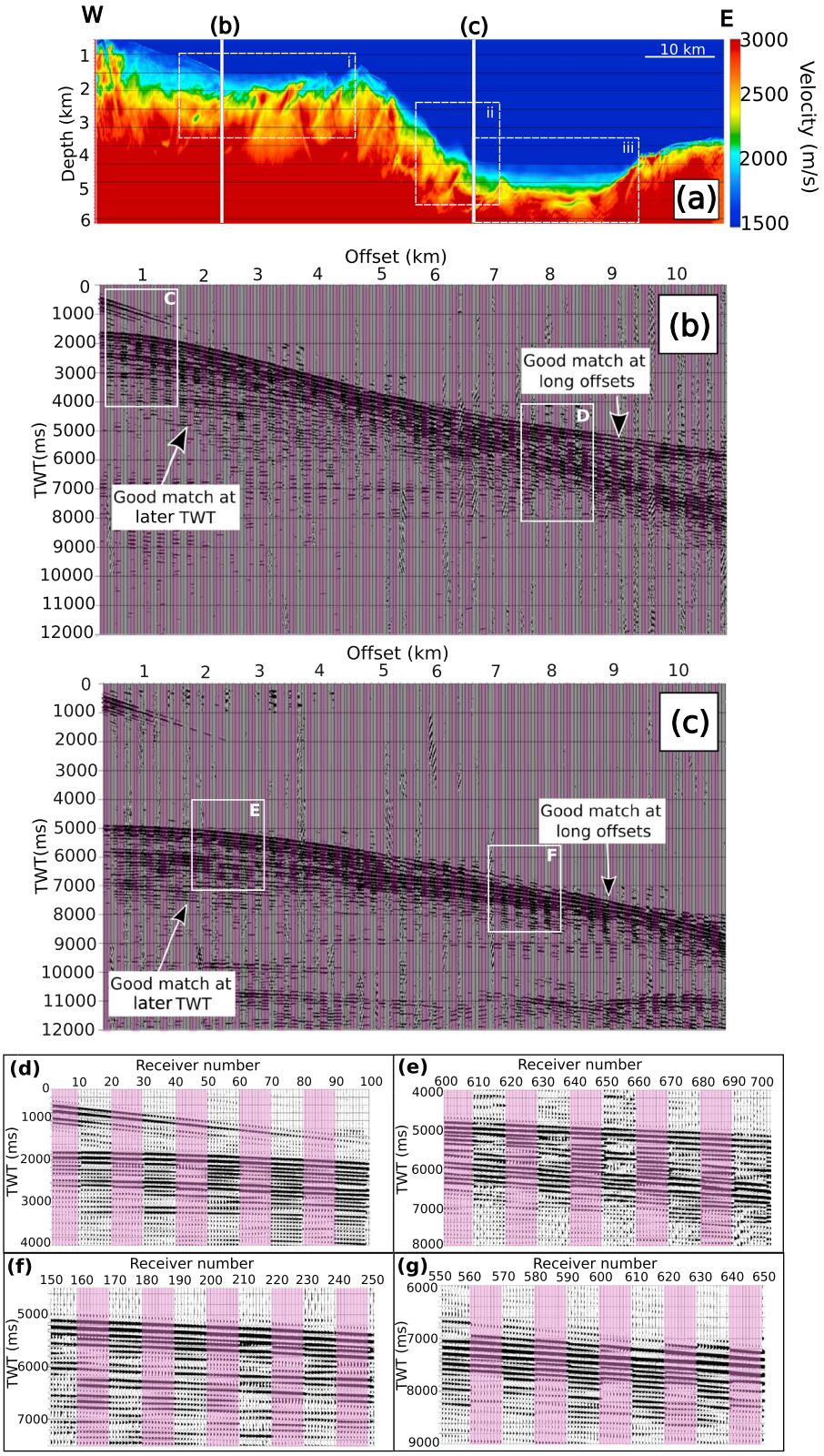

Figure 8. (a) The final *P* wave velocity model produced by FWI. (b) and (c) show the same two shots gathers as Figure 7, with the observed and synthetic data interleaved. In this figure the synthetic data (highlighted in pink) are generated using the final FWI velocity model shown in (a). (d), (e), (f), and (g) show zoomed in plots of data from within the boxes shown in (b) and (c), at the same streamer positions as in Figure 7. These plots show that there is an improvement in the match between the synthetic and observed data, in comparison to the synthetics shown in Figure 7.

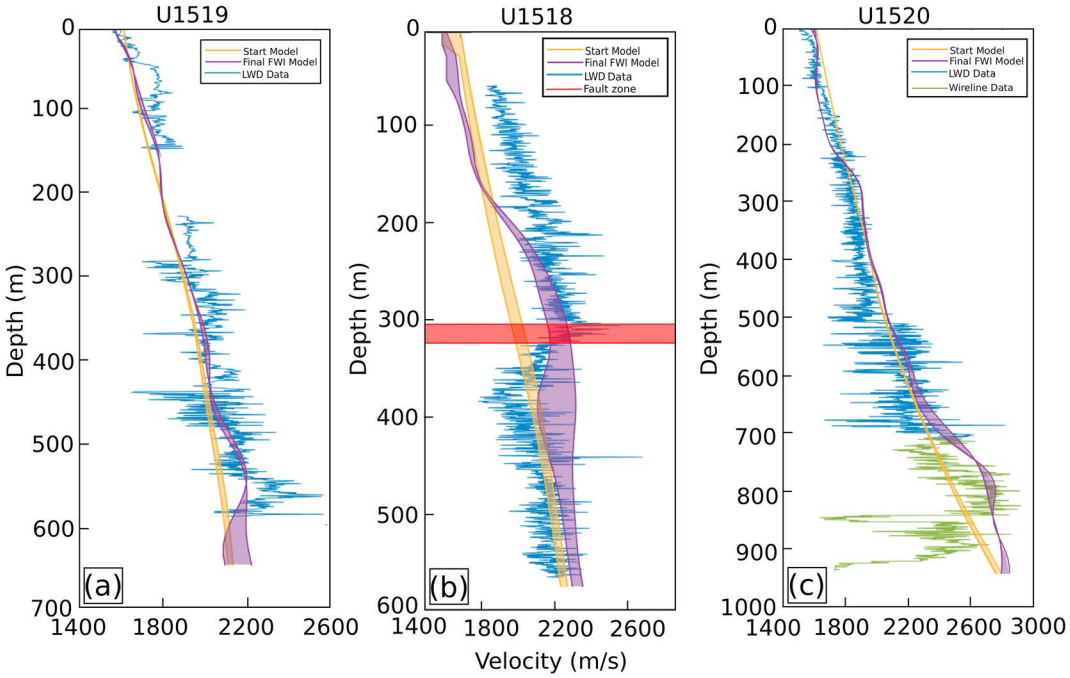

Figure 9. *P* wave velocity at the IODP Expedition 372 drill sites: (a) 1519; (b) 1518, and (c) 1520. Blue lines show LWD data, and green line shows wireline data collected at 1520 on Expedition 375. Yellow and purple lines are the velocities through the starting and FWI velocity models, within a region that extends 100 m either side of the drill site. Red rectangle in (b) shows the location of the fault identified in Saffer et al. (2018).

The LWD tool is most sensitive to vertical changes in velocity, while FWI, determined by refracted turning waves, is more sensitive to horizontal velocities (Figure 6). This means that it is not a straightforward comparison between the LWD data and the velocity data produced by FWI. As the full-waveform inversion is isotropic (Table 1), any anisotropy in the subsurface geology will not be accounted for. This means that we expect to see differences in the size and depth of velocity anomalies within sonic velocity data and the FWI velocity model. As the model converges during inversion, any overestimation or underestimation of velocities, which are due to anisotropy in the shallower parts of the model, will produce offsets between the FWI and well-log velocity-depth structure at deeper depths. The FWI velocity model has a lower resolution than the sonic data, which means that we are not expecting the FWI model to reproduce the fine-scale detail within the sonic log. The sonic data are also collected with much higher frequencies (1–20 kHz) than those used in the inversion (3–8 Hz), which will cause different behaviors between the two techniques, especially in highly porous zones. The final velocities produced by FWI do, however, better match the sonic velocities compared to the starting velocity model. As the drilling occurred post-FWI modeling, we were unable to incorporate the well data into the creation of a starting model. However, it is important to note that comparison between the FWI model created with no available drilling data and the data collected during Expeditions 372 and 375 has shown that FWI is a useful imaging tool for the subsurface structure even in the absence of drilling data.

5.1.4. Quality Assurance: Summary

Although the quality assurance tests presented in sections 5.1.1 to 5.1.3 suggest that our FWI model is an improvement on the starting model, we recognize that our testing is not exhaustive, and the fit between the observed and synthetic data remains imperfect (Figure 8). The most significant contributor to any inaccuracies in our final *Vp* model will likely arise from modeling a 3-D world with a 2-D data set, something we cannot avoid with single streamer data. As there is a newly acquired, 3-D, high-resolution streamer, OBS, and land data set, we have the potential to significantly improve the *Vp* model in 3-D in the future. In addition, since we use several approximations when propagating the seismic wavefield (see section 4), we should expect there to be some inaccuracies and artifacts in the recovered FWI velocity model. Velocity anomalies below the resolution of the inversion (a maximum inversion of 8 Hz would give a resolution of ~140 m in material with *P* wave velocities of ~2,200 m/s) will also not be displayed in the final model but exist in the

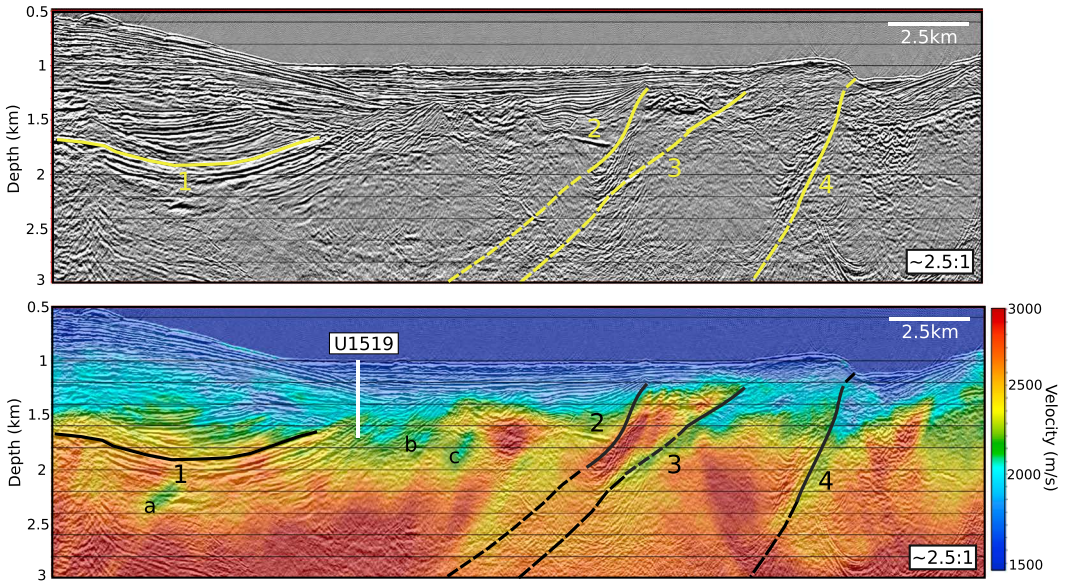

Figure 10. Detailed view of the PSDM seismic image from Barker et al. (2018) and the overlay of the velocity model onto the PSDM seismic image shown in Figure 7i, showing the location of site U1519. This is the overriding plate and a synform has been highlighted, labeled 1, as well as three faults labeled 2, 3, and 4, as well as smaller anomalies labeled a, b, and c, which correspond to shallow gas anomalies associated with the bottom simulating reflection as interpreted by Navalpakam et al. (2012).

true geology within smaller features such as faults, as evidenced by core data (Pecher et al., 2019; Wallace et al., 2019). However, the FWI model does produce a geologically realistic model that better fits drilling data than the starting model. Therefore, we now discuss the recovered velocity anomalies in the context of the geology of the margin.

5.2. Observations From the FWI Velocity Model

5.2.1. The Overriding Plate

We first look at Area i (Figure 7b), which is within the overriding plate above the plate boundary fault that experiences SSEs. In the west of the section we see several strong reflections, most notably a synformal structure at ~1,700 mbsf consisting of several bright, continuous reflections, labeled 1 in Figure 10. When we overlay the FWI velocity model over the seismic reflection section, we see that higher velocities of ~2,500 m/s track these reflections for ~5 km across their entire length (Figure 10). Also, of note are three faults in the reflection seismic section, labeled 2, 3, and 4 in Figure 10. On the overlay plot these faults are coincident with abrupt changes in velocity within the FWI model, which were not apparent in the smoothed starting velocity model. Faults 3 and 4 (Figures 7 and 10) correspond to zones of reduced velocity, with values of ~2,000–2,200 m/s down to depths of ~2,000 and 2,250 mbsf, respectively. These low-velocity zones have a width of ~500 $\pm$ 100 m and are surrounded by rocks with velocities of ~2,500–2,800 m/s. For Fault 2, there is a velocity contrast between the footwall and the hanging wall of up to ~700 m/s between 500 and 1,500 mbsf, with velocities of ~2,500 m/s in the hanging wall and higher velocities (2,900 m/s) in the footwall.

There are some small, unusually low velocity anomalies within the FWI model, for example, below the synform labeled a in Figures 10b and 10c between the U1519 and Fault 2. While these at first appeared anomalous, they correlate extremely well with shallow gas anomalies associated with the bottom simulating reflections as interpreted by Navalpakam et al. (2012; Figure 10) along 05CM-04 using a combination of rock physics modeling and seismic analysis. Wang et al. (2017) also interpreted reduced seismic velocity zones as free gas zones beneath bottom simulating reflections, elsewhere along the margin and similar to the feature labeled a in Figure 10. We therefore consider these small-scale features as real and not artifacts of the inversion.

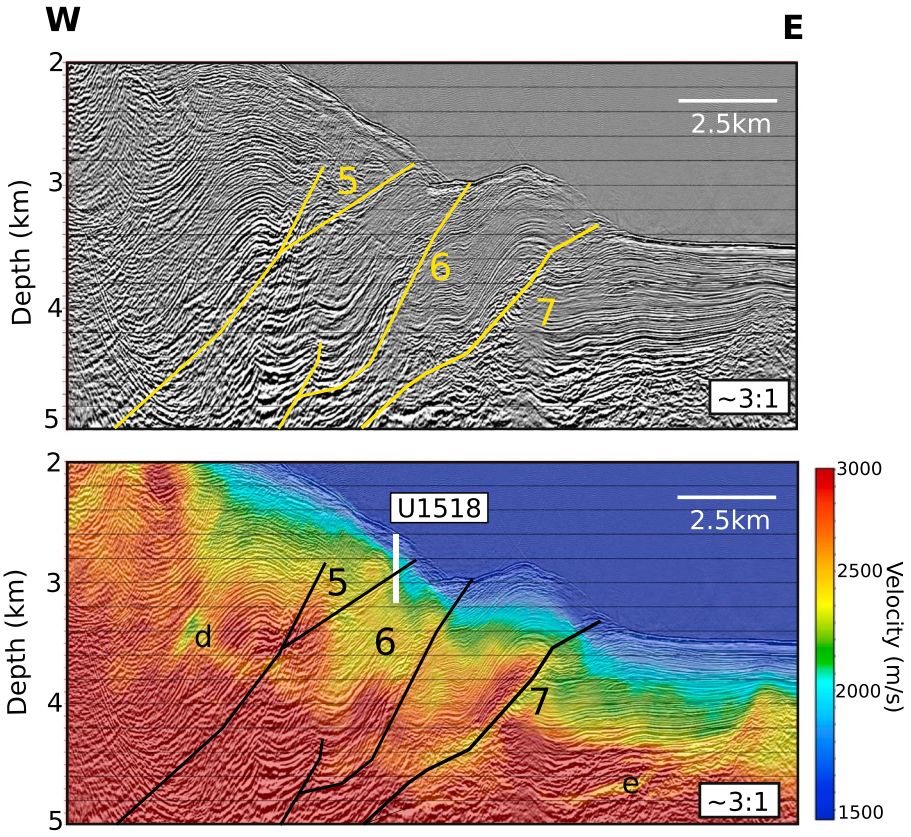

Figure 11. Detailed view of the PSDM seismic image from Barker et al. (2018) and the overlay of the velocity model onto PSDM seismic image shown in Figure 7ii and the location of site U1518. This is the toe of the décollement where three faults have been highlighted labeled 5, 6, and 7 (Barker et al., 2018) and potential inversion artifacts labeled d and e. A package of material of approximately the same velocity has been traced across Fault 6, highlighted by the dashed white lines.

5.2.2. The Toe of the Wedge

The wedge toe is associated with an imbricate stack of faults and associated folds. Fault interpretation is based on Barker et al. (2018) and updated using the reflection data and final FWI velocity model. The seismic reflection profile in Figure 11 shows three reverse splay faults labeled 5, 6, and 7. To the east of Fault 7, we see flat-lying reflections of sediments and sedimentary rocks beneath the Hikurangi Trough, which is shown in more detail in Figure 12. Fault 7 is the first mapped fault and is presumably the youngest in the accretionary wedge. Fault 7 is associated with a low-velocity zone in the final FWI model (Figure 11), which shows a sharp drop in the modeled velocity from ~3,000 m/s in the hanging wall to ~2,300 m/s within the footwall at depths of 900 to 1,200 mbsf. It appears that a low-velocity channel exists in the region where Fault 7 can be mapped in the reflection data. This channel has a velocity of 2,300 m/s, and it separates hanging wall and footwall rocks with velocities of around 2,800 m/s. In the FWI model this low-velocity zone extends down to ~1.5 km bsf (~4.5-km absolute depth in Figure 11) but cannot be resolved any deeper.

In the general region of the toe of the wedge (Figure 11), velocity increases gradually from ~1,600 to 2,300 m/s between 0 and 1,000 mbsf, and the velocity structure follows the general trend of the reflections. Below 1,000 mbsf, both the seismic reflection and velocity model gain complexity. Faults 5 and 6 differ from Faults 2, 3, 4, and 7 in that they appear not to be associated with a discrete low-velocity channel around the fault zone, but rather a moderate velocity contrast between the footwall and hanging wall. Site U1518 drilled through Fault 5 (Fagereng et al., 2019; Figure 11) and LWD sonic velocities decrease below the fault zone (see Figure 9c) from ~2,550 to ~1,900 m/s. This reduction in velocity was not observed within the starting velocity model, shown in yellow in Figure 9b but is partially recovered by FWI.

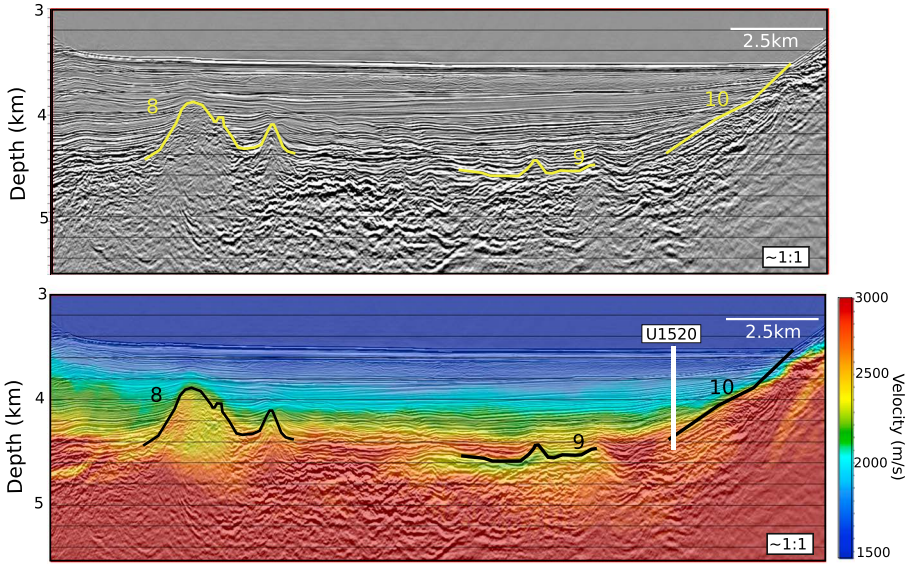

Figure 12. Detailed view of PSDM seismic image from Barker et al. (2018) and the overlay of the velocity model onto the PSDM seismic image shown in Figure 7iii. This is the Hikurangi Trough on the incoming plate, where well U1520 is located. The final model shows two dome-like features of higher velocity, labeled 8, a low-velocity feature labeled 9, and an area of onlapping labeled 10. The velocity inversion west of U1520 highlighted as 9 does correspond to a strong reflector in the PSDM seismic image; however, as the well did not penetrate this zone, we cannot say for sure whether this feature is real or an artifact of the inversion. Nevertheless, synthetic shot gathers in the region match well with real field data, indicating that this feature could be real.

There are some potential artifacts in the final FWI model, for example, the low-velocity anomalies with values between 2,200 and 2,400 m/s labeled d to the left of Fault 5 and e to the right of Fault 7. We suspect that these are artifacts as they do not directly match reflections in the depth-migrated section. As these features are quite small (<100 m), we do not see a mismatch between the real and synthetic shot gather that we can directly correlate with these features (Figure 8c). However, unlike unconstrained anomalies, we do not see any raypath-like shape to these anomalies, so they may be real features. Without direct drilling data at these anomalies, we cannot say for certain whether they are real features or not.

5.2.3. The Incoming Section

An enlargement of the image across the incoming plate, labeled iii in Figure 7b, is shown in Figure 12. In the reflection profile the trench wedge has a horizontally layered stratigraphy, which onlaps two dome-like features (labeled 8 in Figure 12), which were not present in the starting model (Figure 6a). The final FWI velocity model introduces more stepped changes in velocity compared to the starting model, as well as more abrupt changes around features such as feature 8, which exhibits a rapid increase in velocities (~2,500 m/s) compared to the surrounding velocity structure. A low-velocity feature also becomes apparent at ~4.5-km depth in the center of Figure 12, labeled 9, with a velocity of ~2,200 m/s within surrounding velocities of ~2,600 m/s. This low-velocity feature appears to correspond to a strong reflection, to the right of which we see a small high-velocity anomaly with amplitudes of ~3,300 m/s within the surrounding volume. Synthetic shot gathers in the region match well with real field data, however, indicating that this feature could be real. The east of Figure 12 shows a sharp change in velocity, labeled 10, and when overlain with the seismic section we can clearly see the slower sedimentary material of the trough, shown in blues and greens, onlapping onto the faster material of the Tūranganui Knoll seamount shown in oranges and reds. The velocity inversion at 850 mbsf in the wireline log (Figure 9c) coincides with this feature but is not seen as strongly in the final FWI model.

6. Discussion

6.1. Lithology of the Incoming Section

The final *P* wave FWI velocity model reveals the fine-scale velocity structure across the trench wedge (Figures 7 and 12). Velocities range from ~1,700 m/s near the seafloor and gradually increase to ~3,000

m/s at depths of ~2,000 mbsf. Preliminary reports from IODP Expedition 372 and 375 have determined six lithostratigraphic units in this area, consisting of turbidites, mass transport deposits, and hemipelagic muds down to 509.82 mbsf, pelagic carbonate facies from 509.82 to 848.45 mbsf, volcaniclastics from 848.45 to 1,016.24 mbsf and a blend of volcaniclastics, mudstone, limestone, and siltstone down to 1,045.75 mbsf (Wallace et al., 2019). The final FWI model is consistent with these findings as around site U1520 there are distinct changes in velocities at similar depths (Figure 12). We suggest that we can track these lithologies extracted from core data across the trough, away from the well toward the deformation front. The low-velocity zone labeled 9 in Figure 12 approximately corresponds with the feature labeled e in Figure 10, as well as the velocity inversion from the wireline data at ~850 mbsf (Figure 9c). This may suggest spatial variability within the top of the HKB unit across the basin floor. These lithologies could be part of the sedimentary package that surrounds the subducting seamounts. The ~600-m-thick features at the base of the trench wedge at about 4,000 mbsf (labeled 8 in Figure 12) have previously been interpreted as volcanic domes, which are part of a larger seamount complex, which includes the Tūranganui Knolls (Figure 1; Barker et al., 2018). These domes have too low a velocity (~2,500 m/s) to be pure basalt; thus, it is more likely that they are formed from volcaniclastic material or highly altered, fractured basalt. This interpretation is consistent with measured velocities of volcaniclastic sediments within the drill hole, which had significant scatter and ranged in value from 1,800 to 5,000 m/s (Wallace et al., 2019).

6.2. Low-Velocity Zones, Faults, and Fluid Flow

Velocity contrasts between the footwall and hanging wall of some faults in the model (e.g., Faults 3 and the upper part of Fault 7 between 900 and 1,200 mbsf) likely indicate underconsolidated, lower velocity sediments in the footwall compared to the hanging wall, which is now overconsolidated at its current depth, causing velocities to be higher. The availability of drilling data and our high-resolution FWI velocity model will allow models of porosity, effective stress, and pore fluid pressure to be developed in the future to test this hypothesis.

In addition, some splay faults visible in the reflection data correlate with low-velocity zones (reductions of ~500 m/s) in the *P* wave velocity model (Figure 10 Faults 3 and 4). This phenomenon is not unique to Hikurangi; such a relationship has also been noted from waveform tomography across the Nankai subduction zone in Japan where the megasplay fault system interpreted from the reflection image correlates with a sharp *P* wave velocity reduction of ~500–1,000 m/s (Kamei et al., 2012). Lower velocities in the shear zone of the megasplay fault system at Nankai have been identified as potential fluid conduits (Kamei et al., 2012), and this interpretation is supported by the observation of fluid seeps identified by submersibles above faults that have reversed polarity (Park et al., 2002). The low-velocity zones resolved along some faults at Hikurangi may indicate that these are zones of high porosity, which may be maintained by fluid throughput from depth. The interpretation of fluid flow, potentially along faults, is supported by elevated heat flow (Antriasian et al., 2018) and the observation of a number of fluid flow features in the vicinity of seismic line 05CM-04 near the frontal thrust, including pockmarks, flares, and mounds. Porosity values across Fault 5 increase by ~5% within the fault and ~15% below the fault (Pecher et al., 2019; Wallace et al., 2019). Across faults with larger velocity reductions (e.g., Faults 3,4, 5, and 7), however, we predict larger porosity increases due to the lower *P* wave velocities recovered by FWI, leading to the possible presence of fluid and relatively unconsolidated footwall sequences.

The third splay fault in the system (Fault 5 in Figure 11) was drilled by Expeditions 372 and 375 (Fagereng et al., 2019; Pecher et al., 2019; Wallace et al., 2019). This fault is associated with a velocity decrease of ~100 m/s in the FWI model, and the LWD data show the fault (Figure 9b—red region) occurring above a velocity inversion between ~300 and 400 mbsf (Figure 9b). IODP drilling has revealed a zone of intense deformation, between 304.5 and 322.4 mbsf (Fagereng et al., 2019; Figure 9b). If there is only a velocity reduction associated with the fault over a ~20-m-thick region, it will be below the resolution of the FWI model (~140 m in material with *P* wave velocities of ~2,200 m/s at up to 8 Hz). This velocity reduction below the fault zone in the top of the footwall is small compared to the ~700m/s velocity decrease observed along other faults in the FWI model (e.g., Fault 7 in Figure 11) but is consistent with shipboard measurements of decreased porosity below the fault (Pecher et al., 2019; Wallace et al., 2019). This drilled fault may therefore not be acting as a conduit for fluid flow in the same way as other faults, which are associated with discrete, low-velocity anomalies that follow faults mapped in the seismic reflection data (Faults 2, 3, 4, and 7). Fault age may

also play a part in why a low-velocity zone is observed below Fault 7, but not below Faults 5 and 6 (Figure 11). As Fault 7 is likely to be the youngest in the sequence, subducting sediments may be less consolidated here, and/or be in the process of dewatering along the fault as the overburden increases, resulting in the presence of a low-velocity zone.

6.3. Relation to SSEs

SSEs have been associated with low-velocity zones along the megathrust (<35-km depth) in several margins including Cascadia (Audet et al., 2009), Nankai (Kamei et al., 2012; Kodaira et al., 2004), and Costa Rica (Saffer et al., 2000; Tobin et al., 2001). Unfortunately, the limited shot-receiver offset of the data set means that we could not image down to the slow-slip zone in this study due to the limited data recorded by the wavefield penetrating these depths (Figure 6). While we cannot constrain the model down to the SSE zone (Figure 1), we do image the plumbing system above the plate interface, which is known to accommodate SSEs, and IODP Expedition 372 have successfully installed an observatory within Fault 5, which will monitor physical properties across the fault during SSEs to determine whether these events propagate along splay faults in the shallower parts of the margin. Future results from this observatory may reveal that we have, in fact, imaged slowly slipping faults; however, this cannot be confirmed presently. The HRZ-2 SSE source region at a depth of 4 km, shown by high-amplitude reflectivity in Figure 1c, is a target of newly acquired, long-azimuth OBS data collected as part of the NZ3D experiment in January–February 2018.

Another factor suggested to control SSEs is a heterogeneous stress field caused by varying frictional properties at the interface (Peng & Gomberg, 2010). This is often associated with rough subducting seafloor and heterogeneous lithologies within the fault zone (Saffer & Wallace, 2015; Todd, 2017). As outlined in section 6.1, we do see a variation in the *P* wave velocity within the incoming section, which may be indicative of variations in lithology, as well as the presence of volcanic cones (Barker et al., 2009; Barker et al., 2018; Bell et al., 2014). The geological processes responsible for these variable velocities could well influence the stress field at the plate interface and encourage SSEs.

While the 2-D FWI modeling we have presented in this paper gives insight into some of these mechanisms, the upcoming results of the NZ3D seismic experiment, the IODP drilling Expeditions 372 and 375, and the permanent observatories installed at the interface will help to improve understanding of the processes at work at the Hikurangi margin. The performance of FWI improves significantly in 3-D, and full-waveform inversions of the newly acquired 3-D seismic data set will allow us to obtain a more accurate velocity model and image deeper targets. Future work will include the downward continuation of first arrivals, the incorporation of anisotropy and attenuation in our 3-D FWI inversions, and the creation of a new PSDM image using the 3-D FWI velocity model.

7. Conclusion

We have demonstrated that FWI is a useful tool in exploring the physical properties of subduction margins at a high resolution, and the imaging technology can be used effectively even in areas of very deep water and structural complexity. The model has improved on previous velocity models made using PSDM to produce a detailed, geologically realistic model across the shallow subsurface of the margin, which reveals details of the incoming lithology and fault plumbing system above a zone of shallow slow slip.

The high-resolution velocity model allows lithologies in the incoming section to be interpreted from drill site U1520 toward the deformation front. This reveals the inputs into the subduction zone as a combination of pelagics and volcaniclastics and volcaniclastic domes. The FWI velocity model also contains several low-velocity zones that are coincident with faults and their footwall sequences. Velocity changes across the faults from higher-velocity hanging walls to lower velocity footwalls (Faults 3, 4, and upper parts of Fault 7) indicate that the footwall of some faults is underconsolidated, while the hanging wall is overconsolidated for its current depth. Low-velocity channels along faults (Faults 3, 4, and 7) likely indicate high porosity, which may be maintained through the transport of fluids from the subduction interface along these faults. This study has provided a framework for the future application of 3-D FWI to recently acquired, longer-offset, seismic data to recover high-resolution physical properties in zones of slow slip directly.

Acknowledgments

The authors declare that they have no conflict of interest. Data supporting the conclusions made in this contribution can be obtained through the references provided. This research was supported by NERC Grants NE/M021203/1 and NE/S00291X/1. M. Gray's PhD is funded by Imperial College Department of Earth Science and Engineering and the FULLWAVE research group. The authors would like to thank the Imperial College London FULLWAVE group providing the full-waveform inversion code used in this contribution, as well as GNS Science, New Zealand, for providing the data used in the inversions. We would additionally like to thank the International Ocean Discovery Program Expeditions 372 and 375 for providing the well data used in this contribution (now available through IODP at http://iodp.tamu.edu/scienceops/expeditions/hikurangi_gas_hydrate_slides.html and http://iodp.tamu.edu/scienceops/expeditions/hikurangi_subduction_margin.html). In particular, we would like to thank Mike Warner and Tenice Nangoo for technical discussion and Nathan Bangs for comments on the interpretation of the model. We would also like to thank Sally Watson and Philip Barnes for discussion regarding fluid seeps in the region.

References

Antriasian, A., Harris, R. N., Tréhu, A. M., Henrys, S. A., Phrampus, B. J., Lauer, R., et al. (2018). Thermal regime of the Northern Hikurangi Margin, New Zealand. *Geophysical Journal International*, *216*(2), 1177–1190.

Asnaashari, A., Brossier, R., Garambois, S., Audebert, F., Thore, P., & Virieux, J. (2013). Regularized seismic full waveform inversion with prior model information. *Geophysics*, *78*(2), R25–R36. https://doi.org/10.1190/geo2012-0104.1

Audet, P., Bostock, M. G., Boyarko, D. C., Brudzinski, M. R., & Allen, R. M. (2010). Slab morphology in the Cascadia fore arc and its relation to episodic tremor and slip. *Journal of Geophysical Research*, *115*, B00A16. https://doi.org/10.1029/2008JB006053

Audet, P., Bostock, M. G., Christensen, N. I., & Peacock, S. M. (2009). Seismic evidence for overpressured subducted oceanic crust and megathrust fault sealing. *Nature*, *457*(7225), 76–78. https://doi.org/10.1038/nature07650

Bangs, N., Moore, G., Gulick, S., Pangborn, E., Tobin, H., Kuramoto, S., & Taira, A. (2009). Broad, weak regions of the Nankai Megathrust and implications for shallow coseismic slip. *Earth and Planetary Science Letters*, *284*(1-2), 44–49. https://doi.org/10.1016/j.epsl.2009.04.026

Bangs, N. L., McIntosh, K. D., Silver, E. A., Kluesner, J. W., & Ranero, C. R. (2014). Fluid accumulation along the Costa Rica subduction thrust and development of the seismogenic zone. *Journal of Geophysical Research: Solid Earth*, *10*, 67–86. https://doi.org/10.1002/2014JB011265

Bangs, N. L., Shipley, T. H., Moore, J. C., & Moore, G. F. (1999). Fluid accumulation and channeling along the northern Barbados Ridge decollement thrust. *Journal of Geophysical Research*, *104*(B9), 20,399–20,414. https://doi.org/10.1029/1999JB900133

Barker, D. H., Henrys, S., Caratori Tontini, F., Barnes, P. M., Bassett, D., Todd, E., & Wallace, L. (2018). Geophysical constraints on the relationship between seamount subduction, slow slip and tremor at the north Hikurangi subduction zone, New Zealand. *Geophysical Research Letters*, *45*, 12,804–12,813. https://doi.org/10.1029/2018GL080259

Barker, D. H. N., Sutherland, R., Henrys, S., & Bannister, S. (2009). Geometry of the Hikurangi subduction thrust and upper plate, North Island, New Zealand. *Geochemistry, Geophysics, Geosystems*, *10*, Q02007. https://doi.org/10.1029/2008GC002153

Barnes, P., Pecher, I., & LeVay, L. (2017). Expedition 372 Scientific Prospectus: Creeping gas hydrate slides and LWD for Hikurangi subduction margin.

Barnes, P. M., Ghisetti, F. C., Ellis, S., & Morgan, J. K. (2018). The role of protothrusts in frontal accretion and accommodation of plate convergence, Hikurangi subduction margin, New Zealand. *Geosphere*, *14*(2), 440–468. https://doi.org/10.1130/GES01552.1

Barnes, P. M., Lamarche, G., Bialas, J., Henrys, S., Pecher, I., Netzeband, G. L., et al. (2010). Tectonic and geological framework for gas hydrates and cold seeps on the Hikurangi subduction margin, New Zealand. *Marine Geology*, *272*(1-4), 26–48. https://doi.org/10.1016/j.margeo.2009.03.012

Barnes, P. M., & Mercier de Lépinay, B. M. (1997). Rates and mechanics of rapid frontal accretion along the very obliquely convergent southern Hikurangi margin, New Zealand. *Journal of Geophysical Research*, *102*(B11), 24,931–24,952. https://doi.org/10.1029/97JB01384

Bartlow, N. M., Wallace, L. M., Beavan, R. J., Bannister, S., & Segall, P. (2014). Time-dependent modeling of slow slip events and associated seismicity and tremor at the Hikurangi subduction zone, New Zealand. *Journal of Geophysical Research: Solid Earth*, *119*, 734–753. https://doi.org/10.1002/2013JB010609

Bell, R., Holden, C., Power, W., Wang, X., & Downes, G. (2014). Hikurangi margin tsunami earthquake generated by slow seismic rupture over a subducted seamount. *Earth and Planetary Science Letters*, *397*, 1–9. https://doi.org/10.1016/j.epsl.2014.04.005

Bell, R., Sutherland, R., Barker, D. H. N., Henrys, S., Bannister, S., Wallace, L., & Beavan, J. (2010). Seismic reflection character of the Hikurangi subduction interface, New Zealand, in the region of repeated Gisborne slow slip events. *Geophysical Journal International*, *180*(1), 34–48. https://doi.org/10.1111/j.1365-246X.2009.04401.x

Bentham, H., Morgan, J., & Angus, D. (2018). Investigating the use of 3-D full-waveform inversion to characterize the host rock at a geological disposal site. *Geophysical Journal International*, *215*(3), 2035–2046. https://doi.org/10.1093/gji/ggy386

Bilek, S. L., & Lay, T. (2002). Tsunami earthquakes possibly widespread manifestations of frictional conditional stability. *Geophysical Research Letters*, *29*(14), 1673. https://doi.org/10.1029/2002GL015215

Bilek, S. L., Phillips, W. S., Walter, S. Y., Schwartz, S. Y., Peng, Z., & Rotman, H. M. M. (2014). Temporal and spatial variations of earthquake source parameters within the 2012 Nicoya, Costa Rica $M_w = 7.6$ earthquake rupture zone. Paper presented at the AGU Fall Meeting Abstract.

Collot, J. Y., Lewis, K., Lamarche, G., & Lallemand, S. (2001). The giant Ruatoria debris avalanche on the northern Hikurangi margin, New Zealand: Result of oblique seamount subduction. *Journal of Geophysical Research Solid Earth*, *106*(B9), 19271–19297.

Calvert, A. J., Preston, L. A., & Farahbod, A. M. (2011). Sedimentary underplating at the Cascadia mantle-wedge corner revealed by seismic imaging. *Nature Geoscience*, *4*(8), 545–548. https://doi.org/10.1038/ngeo1195

Carter, L., Manighetti, B., Elliot, M., Trustrum, N., & Gomez, B. (2002). Source, sea level and circulation effects on the sediment flux to the deep ocean over the past 15 ka off eastern New Zealand. *Global and Planetary Change*, *33*(3-4), 339–355. https://doi.org/10.1016/S0921-8181(02)00087-5

Christeson, G., Gulick, S., Morgan, J., Gebhardt, C., Kring, D., le Ber, E., et al. (2018). Extraordinary rocks from the peak ring of the Chicxulub impact crater: P-wave velocity, density, and porosity measurements from IODP/ICDP Expedition 364. *Earth and Planetary Science Letters*, *495*, 1–11. https://doi.org/10.1016/j.epsl.2018.05.013

Christeson, G. L., Morgan, J. V., & Warner, M. R. (2012). Shallow oceanic crust: Full waveform tomographic images of the seismic layer 2A/2B boundary. *Journal of Geophysical Research*, *117*, B05101. https://doi.org/10.1029/2011JB008972

Davy, B., Hoernle, K., & Werner, R. (2008). Hikurangi Plateau: Crustal structure, rifted formation, and Gondwana subduction history. *Geochemistry, Geophysics, Geosystems*, *9*, Q07004. https://doi.org/10.1029/2007GC001855

Davy, B., & Wood, R. (1994). Gravity and magnetic modelling of the Hikurangi Plateau. *Marine Geology*, *118*(1-2), 139–151. https://doi.org/10.1016/0025-3227(94)90117-1

Delescluse, M., Nedimović, M. R., & Louden, K. E. (2011). 2D waveform tomography applied to long-streamer MCS data from the Scotian Slope. *Geophysics*, *76*(4), B151–B163. https://doi.org/10.1190/1.3587219

Dominguez, S., Lallemand, S. E., Malavieille, J., & von Huene, R. (1998). Upper plate deformation associated with seamount subduction. *Tectonophysics*, *293*(3-4), 207–224. https://doi.org/10.1016/S0040-1951(98)00086-9

Doser, D. I., & Webb, T. H. (2003). Source parameters of large historical (1917–1961) earthquakes, North Island, New Zealand. *Geophysical Journal International*, *152*(3), 795–832. https://doi.org/10.1046/j.1365-246X.2003.01895.x

Douglas, A., Beavan, J., Wallace, L., & Townend, J. (2005). Slow slip on the northern Hikurangi subduction interface, New Zealand. *Geophysical Research Letters*, *32*, L16305. https://doi.org/10.1029/2005GL023607

Downes, G., Webb, T., McSaveney, M., Darby, D., Doser, D. I., Chague-Goff, C., & Barnett, A. (2001). The 26 March and 17 May 1947 Gisborne earthquakes and tsunami: Implications for tsunami hazard for the east coast, North Island, New Zealand, International Tsunami Workshop" Tsunami Risk Assessment Beyond 2000: Theory. *Practice and Plans", Moscow, Russia*.

Eberhart-Phillips, D., & Chadwick, M. (2002). Three-dimensional attenuation model of the shallow Hikurangi subduction zone in the Raukumara Peninsula, New Zealand. *Journal of Geophysical Research*, *107*(B2), 2033. https://doi.org/10.1029/2000JB000046

Ellis, S., Fagereng, Å., Barker, D., Henrys, S., Saffer, D., Wallace, L., et al. (2015). Fluid budgets along the northern Hikurangi subduction margin, New Zealand: The effect of a subducting seamount on fluid pressure. *Geophysical Journal International*, *202*(1), 277–297. https://doi.org/10.1093/gji/ggv127

Fagereng, Å., Savage, H., Morgan, J., Wang, W., Meneghini, F., Barnes, P., et al., & and the Expedition 372 and 375 science parties (2019). Mixed deformation styles observed on a shallow subduction thrust, Hikurangi margin, New Zealand. *Geology*. https://doi.org/10.1130/G46367.1

Fagereng, Å., & Sibson, R. H. (2010). Melange rheology and seismic style. *Geology*, *38*(8), 751–754.

Ghisetti, F. C., Barnes, P. M., Ellis, S., Plaza-Faverola, A. A., & Barker, D. H. (2016). The last 2 Myr of accretionary wedge construction in the central Hikurangi margin (North Island, New Zealand): Insights from structural modeling. *Geochemistry, Geophysics, Geosystems*, *17*, 2661–2686. https://doi.org/10.1002/2016GC006341

Greinert, J., Lewis, K., Bialas, J., Pecher, I. A., Rowden, A., Bowden, D., et al. (2010). Methane seepage along the Hikurangi Margin, New Zealand: Overview of studies in 2006 and 2007 and new evidence from visual, bathymetric and hydroacoustic investigations. *Marine Geology*, *272*(1-4), 6–25. https://doi.org/10.1016/j.margeo.2010.01.017

Hamling, I. J., Hreinsdóttir, S., Clark, K., Elliott, J., Liang, C., Fielding, E., et al. (2017). Complex multifault rupture during the 2016 Mw 7.8 Kaikōura earthquake, New Zealand. *Science*, *356*(6334), eaam7194.

Hoernle, K., Hauff, F., van den Bogaard, P., Werner, R., Mortimer, N., Geldmacher, J., et al. (2010). Age and geochemistry of volcanic rocks from the Hikurangi and Manihiki oceanic Plateaus. *Geochimica et Cosmochimica Acta*, *74*(24), 7196–7219. https://doi.org/10.1016/j.gca.2010.09.030

Ikari, M. J., & Saffer, D. M. (2011). Comparison of frictional strength and velocity dependence between fault zones in the Nankai accretionary complex. *Geochemistry, Geophysics, Geosystems*, *12*, Q0AD11. https://doi.org/10.1029/2010GC003442

Kamei, R., Pratt, R. G., & Tsuji, T. (2012). Waveform tomography imaging of a megasplay fault system in the seismogenic Nankai subduction zone. *Earth and Planetary Science Letters*, *317-318*, 343–353. https://doi.org/10.1016/j.epsl.2011.10.042

Kanamori, H. (1972). Mechanism of tsunami earthquakes. *Physics of the Earth and Planetary Interiors*, *6*(5), 346–359. https://doi.org/10.1016/0031-9201(72)90058-1

Kodaira, S., Iidaka, T., Kato, A., Park, J.-O., Iwasaki, T., & Kaneda, Y. (2004). High pore fluid pressure may cause silent slip in the Nankai Trough. *Science*, *304*(5675), 1295–1298. https://doi.org/10.1126/science.1096535

Lauer, R. M., & Saffer, D. M. (2012). Fluid budgets of subduction zone forearcs: The contribution of splay faults. *Geophysical Research Letters*, *39*, L13604. https://doi.org/10.1029/2012GL052182

Lewis, K., & Pettinga, J. (1993). The emerging, imbricate frontal wedge of the Hikurangi margin. *Sedimentary Basins of the World*, *2*, 225–250.

Liu, Y., & Rice, J. R. (2005). Aseismic slip transients emerge spontaneously in three-dimensional rate and state modeling of subduction earthquake sequences. *Journal of Geophysical Research*, *110*, B08307. https://doi.org/10.1029/2004JB003424

Liu, Y., & Rice, J. R. (2007). Spontaneous and triggered aseismic deformation transients in a subduction fault model. *Journal of Geophysical Research*, *112*, B09404. https://doi.org/10.1029/2007JB004930

McCaffrey, R., Wallace, L. M., & Beavan, J. (2008). Slow slip and frictional transition at low temperature at the Hikurangi subduction zone. *Nature Geoscience*, *1*(5), 316–320. https://doi.org/10.1038/ngeo178

Morgan, J., Warner, M., Arnoux, G., Hooft, E., Toomey, D., VanderBeek, B., & Wilcock, W. (2016). Next-generation seismic experiments—II: Wide-angle, multi-azimuth, 3-D, full-waveform inversion of sparse field data. *Geophysical Journal International*, *204*(2), 1342–1363. https://doi.org/10.1093/gji/ggv513

Morgan, J., Warner, M., Collins, G., Grieve, R., Christeson, G., Gulick, S., & Barton, P. (2011). Full waveform tomographic images of the peak ring at the Chicxulub impact crater. *Journal of Geophysical Research*, *116*, B06303. https://doi.org/10.1029/2010JB008015

Mountjoy, J. J., & Barnes, P. M. (2011). Active upper plate thrust faulting in regions of low plate interface coupling, repeated slow slip events, and coastal uplift: Example from the Hikurangi Margin, New Zealand. *Geochemistry, Geophysics, Geosystems*, *12*, Q01005. https://doi.org/10.1029/2010GC003326

Multiwave. (2005). 05CM 2D seismic survey, offshore east coast North Island.

Navalpakam, R. S., Pecher, I. A., & Stern, T. (2012). Weak and segmented bottom simulating reflections on the Hikurangi Margin, New Zealand—Implications for gas hydrate reservoir rocks. *Journal of Petroleum Science and Engineering*, *88*, 29–40.

Park, J.-O., Tsuru, T., Kodaira, S., Cummins, P. R., & Kaneda, Y. (2002). Splay fault branching along the Nankai subduction zone. *Science*, *297*(5584), 1157–1160. https://doi.org/10.1126/science.1074111

Pecher, I. A., Barnes, P. M., LeVay, L. J., & the Expedition 372A Scientists (2019). Creeping gas hydrate slides. In *Proceedings of the International Ocean Discovery Program*, (Vol. 372A). College Station, TX: International Ocean Discovery Program. https://doi.org/10.14379/iodp.proc.372A.2019

Pedley, K. L., Barnes, P., Pettinga, J. R., & Lewis, K. (2010). Seafloor structural geomorphic evolution of the accretionary frontal wedge in response to seamount subduction, Poverty Indentation, New Zealand. *Marine Geology*, *270*(1-4), 199–138.

Peng, Z., & Gomberg, J. (2010). An integrated perspective of the continuum between earthquakes and slow-slip phenomena. *Nature Geoscience*, *3*(9), 599–607. https://doi.org/10.1038/ngeo940

Plaza-Faverola, A., Henrys, S., Pecher, I., Wallace, L., & Klaeschen, D. (2016). Splay fault branching from the Hikurangi subduction shear zone: Implications for slow slip and fluid flow. *Geochemistry, Geophysics, Geosystems*, *17*, 5009–5023. https://doi.org/10.1002/2016GC006563

Plaza-Faverola, A., Klaeschen, D., Barnes, P., Pecher, I., Henrys, S., & Mountjoy, J. (2012). Evolution of fluid expulsion and concentrated hydrate zones across the southern Hikurangi subduction margin, New Zealand: An analysis from depth migrated seismic data. *Geochemistry, Geophysics, Geosystems*, *13*, Q08018. https://doi.org/10.1029/2012GC004228

Pratt, R. G. (1999). Seismic waveform inversion in the frequency domain. Part 1: Theory and verification in a physical scale model. *Geophysics*, *64*(3), 888–901. https://doi.org/10.1190/1.1444597

Rogers, G., & Dragert, H. (2003). Episodic tremor and slip on the Cascadia subduction zone: The chatter of silent slip. *Science*, *300*(5627), 1942–1943. https://doi.org/10.1126/science.1084783

Rondenay, S., Abers, G. A., & Van Keken, P. E. (2008). Seismic imaging of subduction zone metamorphism. *Geology*, *36*(4), 275–278. https://doi.org/10.1130/G24112A.1

Saffer, D. M. (2003). Pore pressure development and progressive dewatering in underthrust sediments at the Costa Rican subduction margin: Comparison with northern Barbados and Nankai. *Journal of Geophysical Research*, *108*(B5), 2261. https://doi.org/10.1029/2002JB001787

Saffer, D. M., Silver, E. A., Fisher, A. T., Tobin, H., & Moran, K. (2000). Inferred pore pressures at the Costa Rica subduction zone: Implications for dewatering processes. *Earth and Planetary Science Letters*, *177*(3-4), 193–207. https://doi.org/10.1016/S0012-821X(00)00048-0

Saffer, D. M., & Tobin, H. J. (2011). Hydrogeology and mechanics of subduction zone forearcs: Fluid flow and pore pressure. *Annual Review of Earth and Planetary Sciences*, *39*(1), 157–186. https://doi.org/10.1146/annurev-earth-040610-133408

Saffer, D. M., & Wallace, L. M. (2015). The frictional, hydrologic, metamorphic and thermal habitat of shallow slow earthquakes. *Nature Geoscience*, *8*(8), 594–600. https://doi.org/10.1038/ngeo2490

Saffer, D. M., Wallace, L. M., Petronotis, K., & Scientists, a. t. E. (2018). Expedition 375 Preliminary Report: Hikurangi subduction margin coring and observatories. International Ocean Discovery Program. https://doi.org/10.14379/iodp.pr.375.2018

Sahling, H., Masson, D. G., Ranero, C. R., Hühnerbach, V., Weinrebe, W., Klaucke, I., et al. (2008). Fluid seepage at the continental margin offshore Costa Rica and southern Nicaragua. *Geochemistry, Geophysics, Geosystems*, *9*, Q05S05. https://doi.org/10.1029/2008GC001978

Scholz, C. H. (1998). Earthquakes and friction laws. *Nature*, *391*(6662), 37–42. https://doi.org/10.1038/34097

Seno, T. (2002). Tsunami earthquakes as transient phenomena. *Geophysical Research Letters*, *29*(10), 58-1. https://doi.org/10.1029/2002GL014868

Shibazaki, B., & Iio, Y. (2003). On the physical mechanism of silent slip events along the deeper part of the seismogenic zone. *Geophysical Research Letters*, *30*(9), 1489. https://doi.org/10.1029/2003GL017047

Sirgue, L., Barkved, O., Dellinger, J., Etgen, J., Albertin, U., & Kommedal, J. (2010). Thematic set: Full waveform inversion—The next leap forward in imaging at Valhall. *First Break*, *28*(4), 65–70.

Sirgue, L., & Pratt, R. G. (2004). Efficient waveform inversion and imaging: A strategy for selecting temporal frequencies. *Geophysics*, *69*(1), 231–248. https://doi.org/10.1190/1.1649391

Song, T.-R. A., Helmberger, D. V., Brudzinski, M. R., Clayton, R. W., Davis, P., Pérez-Campos, X., & Singh, S. K. (2009). Subducting slab ultra-slow velocity layer coincident with silent earthquakes in southern Mexico. *Science*, *324*(5926), 502–506. https://doi.org/10.1126/science.1167595

Stockwell, J. W., & Cohen, J. K. (2002). The new SU user's manual. *Center for Wave Phenomena, Colorado School of Mines, Golden, USA*, *3*.

Tarantola, A. (1984). Inversion of seismic reflection data in the acoustic approximation. *Geophysics*, *48*(8), 1259–1266.

Tobin, H., Vannucchi, P., & Meschede, M. (2001). Structure, inferred mechanical properties, and implications for fluid transport in the décollement zone, Costa Rica convergent margin. *Geology*, *29*(10), 907–910. https://doi.org/10.1130/0091-7613(2001)029<0907:SIMPAI>2.0.CO;2

Tobin, H. J., & Saffer, D. M. (2009). Elevated fluid pressure and extreme mechanical weakness of a plate boundary thrust, Nankai Trough subduction zone. *Geology*, *37*(8), 679–682. https://doi.org/10.1130/G25752A.1

Todd, E., Schwartz, S. Y., Mochizuki, K., Wallace, L., Sheehan, A. F., Webb, S. C., et al. (2018). Earthquakes and tremor linked to seamount subduction during shallow slow slip at the Hikurangi Margin, New Zealand. *Journal of Geophysical Research: Solid Earth*, *123*, 6769–6783. https://doi.org/10.1029/2018JB016136

Todd, E. K. (2017). Interplay between modes of strain release along the shallow northern Hikurangi subduction zone, New Zealand. UC Santa Cruz,

Virieux, J., & Operto, S. (2009). An overview of full-waveform inversion in exploration geophysics. *Geophysics*, *74*(6), WCC1–WCC26. https://doi.org/10.1190/1.3238367

Walcott, R. I. (1987). Geodetic strain and the deformational history of the North Island of New Zealand during the late Cainozoic. *Philosophical Transactions of the Royal Society of London. Series A, Mathematical and Physical Sciences*, *321*(1557), 163–181.

Wallace, L. M., Bartlow, N., Hamling, I., & Fry, B. (2014). Quake clamps down on slow slip. *Geophysical Research Letters*, *41*, 8840–8846. https://doi.org/10.1002/2014GL062367

Wallace, L. M., & Beavan, J. (2006). A large slow slip event on the central Hikurangi subduction interface beneath the Manawatu region, North Island, New Zealand. *Geophysical Research Letters*, *33*, L11301. https://doi.org/10.1029/2006GL026009

Wallace, L. M., & Beavan, J. (2010). Diverse slow slip behavior at the Hikurangi subduction margin, New Zealand. *Journal of Geophysical Research*, *115*, B12402. https://doi.org/10.1029/2010JB007717

Wallace, L. M., Beavan, J., Bannister, S., & Williams, C. (2012). Simultaneous long-term and short-term slow slip events at the Hikurangi subduction margin, New Zealand: Implications for processes that control slow slip event occurrence, duration, and migration. *Journal of Geophysical Research*, *117*, B11402. https://doi.org/10.1029/2012JB009489

Wallace, L. M., Beavan, J., McCaffrey, R., & Darby, D. (2004). Subduction zone coupling and tectonic block rotations in the North Island, New Zealand. *Journal of Geophysical Research*, *109*, B12406. https://doi.org/10.1029/2004JB003241

Wallace, L. M., Reyners, M., Cochran, U., Bannister, S., Barnes, P. M., Berryman, K., et al. (2009). Characterizing the seismogenic zone of a major plate boundary subduction thrust: Hikurangi Margin, New Zealand. *Geochemistry, Geophysics, Geosystems*, *10*, Q10006. https://doi.org/10.1029/2009GC002610

Wallace, L. M., Saffer, D. M., Barnes, P. M., Pecher, I. A., Petronotis, K. E., LeVay, L. J., & the Expedition 372/375 Scientists (2019). Hikurangi subduction margin coring, logging, and observatories. In *Proceedings of the International Ocean Discovery Program* (Vol. 372/375). College Station, TX: International Ocean Discovery Program. https://doi.org/10.14379/iodp.proc.372B375.2019

Wallace, L. M., Webb, S. C., Ito, Y., Mochizuki, K., Hino, R., Henrys, S., et al. (2016). Slow slip near the trench at the Hikurangi subduction zone, New Zealand. *Science*, *352*(6286), 701–704. https://doi.org/10.1126/science.aaf2349

Wang, H., Crutchley, G., & Stern, T. (2017). Gas hydrate formation in compressional, extensional and un-faulted structural settings—Examples from New Zealand's Hikurangi margin. *Marine and Petroleum Geology*, *88*, 69–80. https://doi.org/10.1016/j.marpetgeo.2017.08.001

Wang, K., & Bilek, S. L. (2014). Invited review paper: Fault creep caused by subduction of rough seafloor relief. *Tectonophysics*, *610*, 1–24. https://doi.org/10.1016/j.tecto.2013.11.024

Warner, M., Ratcliffe, A., Nangoo, T., Morgan, J. V., Umpleby, A., Shah, N., et al. (2013). Anisotropic 3D full-waveform inversion. *Geophysics*, *78*(2), R59–R80. https://doi.org/10.1190/geo2012-0338.1

Warner, M., Umpleby, A., & Stekl, I. (2010, June). 3D full-wavefield tomography: imaging beneath heterogeneous overburden. In 72nd EAGE Conference and Exhibition-Workshops and Fieldtrips.

Wech, A. G., Creager, K. C., & Melbourne, T. I. (2009). Seismic and geodetic constraints on Cascadia slow slip. *Journal of Geophysical Research*, *114*, B10316. https://doi.org/10.1029/2008JB006090
Yilmaz, Ö. (2001). *Seismic data analysis*, (Vol. 1). Tulsa: Society of Exploration Geophysicists.